

Unsupervised Deep Video Denoising

Dev Yashpal Sheth^{1*}, Sreyas Mohan^{2*}, Joshua L. Vincent³, Ramon Manzorro³, Peter A. Crozier³,
Mitesh M. Khapra^{1,6}, Eero P. Simoncelli^{2,4,5}, Carlos Fernandez-Granda^{2,5}

¹ Indian Institute of Technology Madras, India,

² Center for Data Science, New York University,

³ School for Engineering of Matter, Transport, and Energy, ASU,

⁴ Center for Neural Science, and Howard Hughes Medical Institute, NYU,

⁵ Courant Institute of Mathematical Sciences, NYU,

⁶ Robert Bosch Center for Data Science and AI.

Abstract

Deep convolutional neural networks (CNNs) currently achieve state-of-the-art performance in denoising videos. They are typically trained with supervision, minimizing the error between the network output and ground-truth clean videos. However, in many applications, such as microscopy, noiseless videos are not available. To address these cases, we build on recent advances in unsupervised still image denoising to develop an Unsupervised Deep Video Denoiser (UDVD). UDVD is shown to perform competitively with current state-of-the-art supervised methods on benchmark datasets, even when trained only on a single short noisy video sequence. Experiments on fluorescence-microscopy and electron-microscopy data illustrate the promise of our approach for imaging modalities where ground-truth clean data is generally not available. In addition, we study the mechanisms used by trained CNNs to perform video denoising. An analysis of the gradient of the network output with respect to its input reveals that these networks perform spatio-temporal filtering that is adapted to the particular spatial structures and motion of the underlying content. We interpret this as an implicit and highly effective form of motion compensation, a widely used paradigm in traditional video denoising, compression, and analysis. Code and iPython notebooks for our analysis are available in <https://sreyas-mohan.github.io/udvd/>.

1. Introduction

Data acquired from any imaging device is subject to noise that degrades the signal. Video denoising – the restoration of an original video signal from an observed

noisy measurement – is a foundational problem in image processing, as well as an important preprocessing step for computer vision tasks. Convolutional neural networks (CNNs) [20] are the current state-of-the-art for this problem [31, 32]. These networks are typically trained using a database of clean videos, which are corrupted with simulated noise. However, in applications such as microscopy, noiseless ground truth videos are often not available. To address this issue, we propose a method to train a video denoising CNN without access to supervised data, which we call Unsupervised Deep Video Denoising (UDVD).

UDVD is inspired by the “blind-spot” technique, recently introduced for unsupervised image denoising [21, 16, 2, 18], in which a CNN is trained to estimate each *noisy* pixel from the surrounding spatial neighborhood *without including the pixel itself*. Here, we propose a novel blind-spot architecture that processes the surrounding spatio-temporal neighborhood to denoise videos. We show that the approach is competitive with the current supervised state-of-the-art on standard benchmarks, despite the fact that it does not have access to ground-truth clean videos during training. Combined with aggressive data augmentation, it produces high-quality denoising even when trained on very short video sequences of just around 50 frames. In addition, we validate our approach on real-world data from electron microscopy and fluorescence microscopy.

In order to exploit spatio-temporal information in video denoising, it is crucial to account for the movement of objects within the video. Combining noisy pixels across time without taking into consideration such motion would blur the corresponding objects, degrading the denoised signal. Most approaches that use temporal information [22, 1, 3, 23], including those based on deep CNNs [31, 38, 10, 11, 39], use an estimate of the optical flow in the video to adaptively compensate for the motion, allowing proper align-

*equal contribution

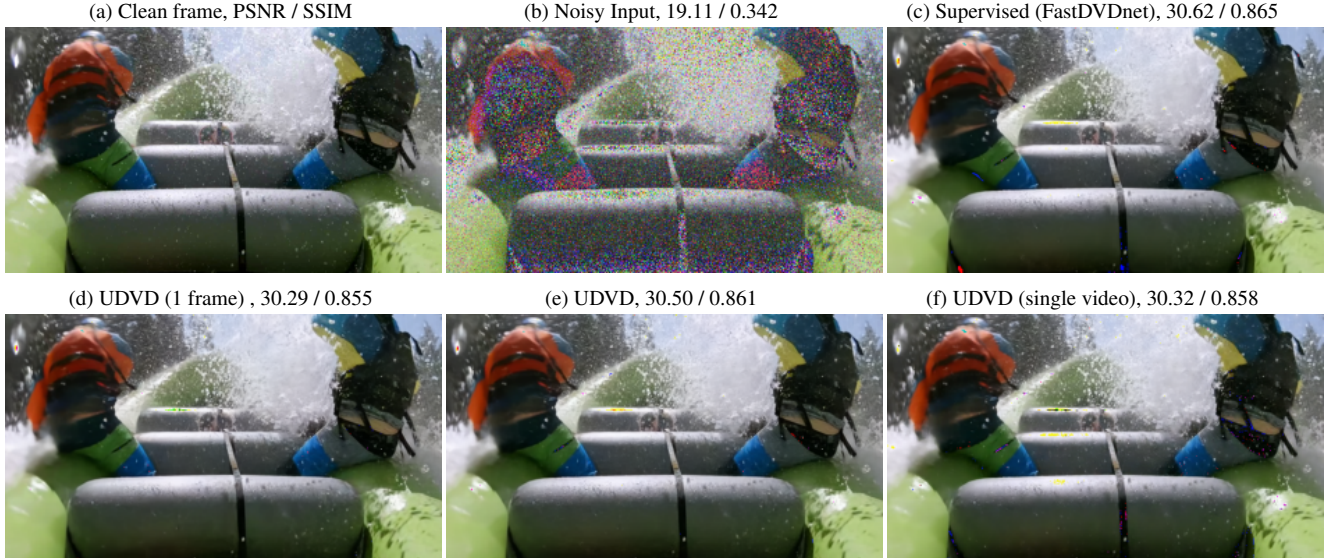


Figure 1. **Unsupervised denoising matches the performance of supervised denoising.** Frame from a video in the Set8 dataset denoised using different approaches. (a) Clean frame. (b) Frame corrupted with Gaussian noise of standard deviation 30 (relative to intensity range [0-255]). (c) FastDVDnet [32], a supervised method trained on the DAVIS dataset. (d) Single-image unsupervised method [18] trained on the DAVIS dataset. (e) Our proposed unsupervised method (UDVD), which uses five frames to denoise each frame, trained on the DAVIS dataset. (f) UDVD trained only on the noisy video itself. Performance is quantified using PSNR / SSIM [35], respectively. Additional denoised videos are included in our [website](#).

ment and combination of noisy pixels over time. However, several current state-of-the-art methods for video denoising do not perform explicit estimation of the optical flow. They are trained only with clean video signals and their simulated noisy counterparts. This yields excellent empirical performance, but also raises an important question: *How can they succeed without explicit motion compensation?*

Here, we examine the mechanisms learned by CNNs trained for video denoising, by analyzing the gradient of their output with respect to their input. Analysis of this local linear approximation of the denoising map shows that both supervised and unsupervised CNNs perform spatio-temporal adaptive filtering, which is aligned with object motion. Thus, these CNNs are *automatically performing implicit motion compensation*. In addition, we demonstrate that it is possible to estimate optical flow accurately from the network gradients, even though the networks are not provided with any explicit optical flow constraints in their architecture, their objective functions, or their training data.

2. Background and Related Work

Traditional techniques for image denoising include non-linear filtering [33, 24], sparsity-based methods [4, 28, 7], and nonlocal approaches [19]. Many of these techniques have been successfully extended to video denoising [22, 1, 23, 3]. In order to preserve the spatiotemporal structure of the objects in the video, these methods rely on motion compensation, typically using an estimate of the optical flow.

In the last five years, data-driven methods based on deep CNNs [20] have outperformed all other techniques in image denoising [42, 12, 5]. The CNNs are trained to minimize the mean squared error between the network output and clean images using large databases of natural images. This framework has been recently applied to video data, also achieving state-of-the-art performance [31, 38, 32, 40, 10].

As in the case of prior methodology, many deep-learning techniques for video denoising perform explicit motion compensation. DVDnet [31] applies an image-denoising CNN to each input frame, estimates the optical flow from the denoised frames using DeepFlow [36] (a deep CNN model pretrained for this purpose), warps the frames using the flow estimate to align their content, and finally processes the registered frames with a CNN. Ref. [38] applies a similar pipeline, but incorporates an optical-flow estimation module, which is jointly trained end-to-end together with the denoising CNN.

Three recent methods perform video denoising without explicit motion estimation. VNLnet [8] uses a non-local search algorithm to find self-similar patches in the input video, and then uses a CNN to process the patches. ViDeNN [6] consists of a first stage that denoises each frame using a residual CNN similar to DnCNN [42], and a second stage that exploits temporal structure by using the $(t-1)^{th}$, t^{th} , $(t+1)^{th}$ frames to produce the denoised t^{th} frame. FastDVDnet [32] uses UNet [30] blocks, trained end to end, to denoise each frame using five contiguous frames. These

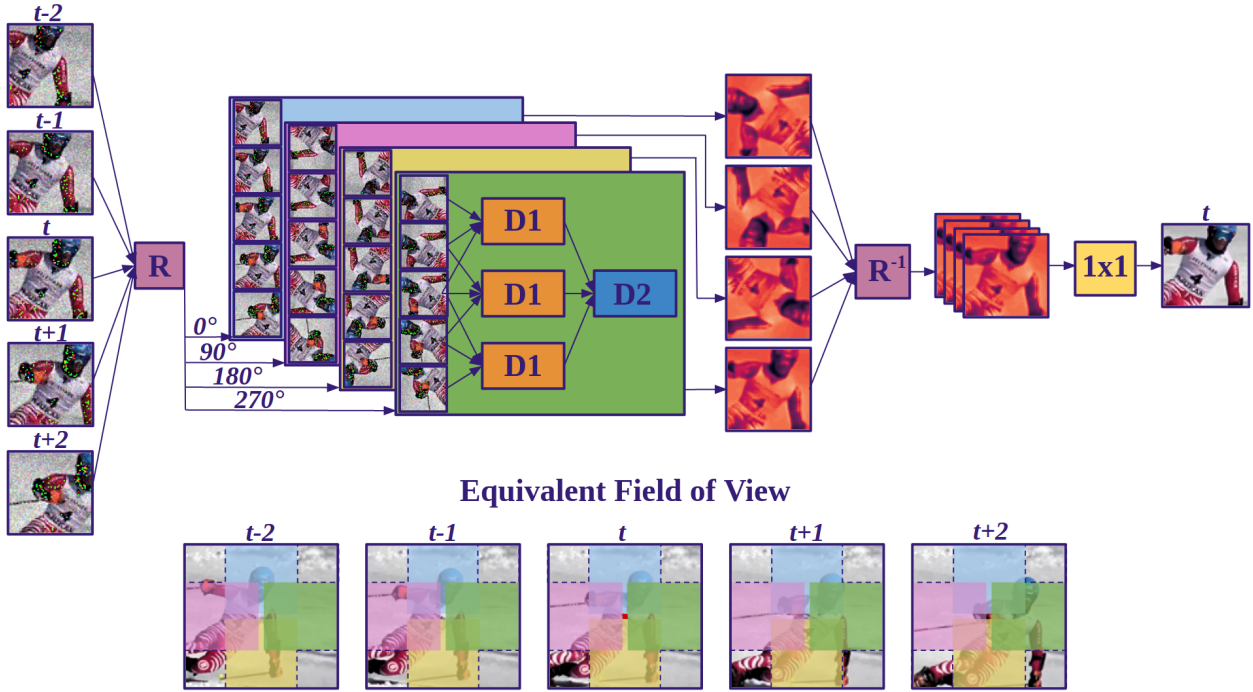


Figure 2. **Unsupervised Deep Video Denoising (UDVD) Network Architecture.** The network takes 5 consecutive noisy frames as input and produces a denoised central frame as output. We rotate the input frames by multiples of 90° and process them in four separate branches with shared parameters, each containing asymmetric convolutional filters that are *vertically causal*. As a result, the branches produce outputs that only depend on the pixels above (0° rotation, blue region), to the left (90° , pink region), below (180° , yellow region) or to the right (270° , green region) of the output pixel. Each branch uses a 2-stage cascade of Unet-style blocks (D1 and D2) to combine information over frames. These outputs are then *derotated* and linearly combined (using a 1×1 convolutions) followed by a ReLU nonlinearity to produce the final output. The resulting “field of view” is depicted at the bottom with each color representing the contribution of the corresponding branch.

methods achieve state-of-the-art performance without any explicit motion compensation. In this work we show that such CNNs actually performs *implicit* motion estimation, which can be revealed through a gradient-based analysis.

The deep-learning approaches described above all rely on the availability of ground-truth clean videos to train the models in a supervised manner. However, such data may not be available in practical applications, such as medical or scientific imaging. In addition, the interactions between realistic noise processes and the video signal may not be adequately reflected by corrupting clean videos with simulated noise (often chosen to be additive and Gaussian). This is illustrated by the results in [40], where realistic clean-noisy pairs are created by moving controllable objects and averaging each static moment multiple times to generate clean frames. A CNN trained on such data is shown to outperform approaches trained using simulated noise. However, constructing such datasets is not feasible for many applications, where there is no model for the movement of the objects of interest. This motivates development of a fully unsupervised methodology, which does not require access

to ground-truth clean videos.

Noise2Noise is an unsupervised image-denoising technique where a CNN is trained on pairs of noisy images corresponding to the same clean image [21]. Frame2Frame [10] exploits this approach to fine-tune a pre-trained image-denoising CNN with noisy data. The idea is to register contiguous frames using an estimate of the optical flow (obtained from TV-L1 [41]), and treat them as noisy realizations of the same clean image, taking into account an estimate of occlusions between frames. This scheme is extended to have a trainable flow estimation module in [39] and to use multiple noisy frames as input in [9]. Ref. [11] proposes an alternative approach to produce aligned noisy frames, and improves occlusion estimation using optical-flow consistency.

Using the Noise2Noise framework to perform unsupervised video denoising requires warping adjoining frames, so that they correspond (as much as possible) to the same underlying image. This in turn requires explicit motion compensation, and accurate occlusion estimation. In addition, the assumption that contiguous frames can be suc-

test set	σ	Traditional		Supervised CNN			Unsupervised CNN (UDVD)		
		VNLB	VBM4D	VNLnet	DVDnet	FastDVDnet	1 frame	3 frames	5 frames
DAVIS	30	33.73	31.65	-	34.08	34.06	32.79	33.42	33.86
	40	32.32	30.05	32.32	32.86	32.80	31.47	32.15	32.61
	50	31.13	28.80	31.43	31.85	31.83	30.46	31.15	31.63
Set8	30	31.74	30.00	-	31.79	31.60	30.68	31.46	31.86
	40	30.39	28.48	30.55	30.55	30.37	29.33	30.18	30.62
	50	29.24	27.33	29.47	29.56	29.42	28.28	29.18	29.63

Table 1. **Denoising results on natural video datasets.** All networks are trained on the DAVIS train set. Performance values are PSNR of each trained network averaged over held-out test data. UDVD, operating on 5 frames, outperforms the supervised methods on Set8 and is competitive on the DAVIS test set. Unsupervised denoisers with more temporal frames show a consistent improvement in denoising performance. DVDnet and FastDVDnet are trained using varying noise levels ($\sigma \in [0, 55]$) and VNLnet is trained and evaluated on each specified noise level. All unsupervised CNNs are trained *only* at $\sigma = 30$, showing that they generalize well on unseen noise levels. See Sections C and E for additional results. The PSNR values for all methods except UDVD are taken from [32]

cessfully registered may not hold, particularly if the motion speeds in the video are large relative to the frame rate. In order to bypass these issues, we develop a blind-spot network that makes it possible to train denoising CNNs by fitting the noisy data. The CNN is trained to estimate each noisy pixel value using the surrounding neighborhood, but without taking into account the noisy value itself in order to avoid the identity solution. This “blind spot” can be explicitly enforced through the architecture design [18], or by masking [2, 16]. The output of the network is then combined with the noisy pixel values via weighted averaging to produce the final denoised estimate. Several variations of this approach have been shown to provide effective denoising of both natural images and real-world noisy images from fluorescence microscopy [17, 29, 14].

3. Unsupervised Deep Video Denoising

In this section we describe our multi-frame blind-spot CNN. Figure 2 shows a detailed diagram of the architecture.

Multi-frame blind-spot architecture. Our CNN maps five contiguous noisy frames to a denoised estimate of the middle frame. Building on the “blind spot” idea proposed in [18] for single-image denoising, we design the architecture so that each output pixel is estimated from a spatiotemporal neighbourhood that does not include the pixel itself. We rotate the input frames by multiples of 90° and process them through four separate branches containing asymmetric convolutional filters that are *vertically causal*. As a result, the branches produce outputs that only depend on the pixels above (0° rotation), to the left (90°), below (180°) or to the right (270°) of the output pixel. These partial outputs are then *derotated* and combined using a three-layered cascade of 1×1 convolutions and nonlinearities to produce the final output. The resulting field of view is depicted at the bottom

of Figure 2.

The structure of the branches that process the groups of five rotated frames is based on architectures previously proposed for supervised video denoising [31, 6], particularly [32]. A first stage, consisting of three UNets [30] (D1 in the diagram) with shared parameters, maps each group of three contiguous frames (i.e. $(t-2, t-1, t)$, $(t-1, t, t+1)$ and $(t, t+1, t+2)$) to a separate feature map. These features are then mapped to a single output using another UNet (D2). The D1 and D2 blocks have two down-sampling layers.

Bias-free architecture. Inspired by [25], we remove all additive terms from the convolutional layers in UDVD. This provides automatic generalization to varying noise levels not encountered during training, and facilitates our proposed analysis to interpret the denoising mechanisms learned by the network (see Section 6 and 7).

Using the missing pixel. The denoised value generated by the proposed architecture at each pixel is computed without using the noisy observation at that location. This avoids overfitting – i.e. learning the trivial identity map that minimizes the mean-squared error cost function – but ignores important information provided by the noisy pixel. In the case of Gaussian additive noise, we can use this information via a precision-weighted average between the network output and the noisy pixel value. Following [18], the weights in the average are derived by assuming a Gaussian distribution for the error in the blind-spot estimates of the (color) pixel values. The CNN architecture is trained to estimate the mean and covariance of this distribution at each pixel by maximizing the log likelihood of the noisy data (see Section A.2 for a detailed formulation).

Data augmentation. An important challenge when performing unsupervised video denoising is the limited availability of training data. In supervised video denoising with simulated noise, training can rely on generation of a vir-

	$\sigma = 30$					$\sigma = 90$				
	snow	tennis-v	hyper	raft	mean	snow	tennis-v	hyper	raft	mean
No. of frames	59	75	37	29	-	59	75	37	29	-
No Augmentation	30.44	33.37	32.26	30.56	31.66	24.11	26.12	25.02	24.68	24.98
Flip	+0.35	+0.89	+0.15	-0.18	+0.30	+1.08	+2.55	+1.89	+1.26	+1.70
Flip + TR	+0.32	+1.04	-0.03	-0.45	+0.22	+1.33	+3.05	+2.14	+1.34	+1.97
Flip + TR + TS	+0.35	+1.24	+0.22	-0.74	+0.27	+1.33	+3.41	+2.33	+1.23	+2.08
UDVD*	+0.35	+1.43	-0.01	+0.29	+0.52	+1.37	+3.43	+1.96	+1.38	+2.04
FastDVDnet*	+0.31	+1.17	+0.14	+0.41	+0.51	+0.90	+2.37	+1.54	+1.03	+1.46

Table 2. **Results for UDVD trained on individual noisy videos.** The top four rows show PSNR values for UDVD trained on each individual video sequence with different data augmentation techniques - a) spatial flipping (Flip), b) time reversal (TR) and c) temporal subsampling (TS). With the full set of augmentations, performance is comparable to that of UDVD or FastDVDnet trained on the full DAVIS dataset (indicated by *). All the PSNR values are reported relative to UDVD trained on the individual without data augmentation (top row). The snowboard, hypersmooth and rafting sequences are from Set8, tennis-vest is from DAVIS.

tually unlimited set of fresh noise realizations, which prevents overfitting. In the unsupervised setting, this is not realistic, raising substantial challenges for effective denoising of short video sequences. To address this, we leverage data augmentation strategies including spatial flipping, time reversal, and temporal subsampling (i.e. skipping intermediate frames). This makes it possible to train UDVD with short video sequences (e.g., 50 frames), while achieving denoising performance that is on par with both unsupervised and supervised networks trained on much larger datasets (see Figure 1 and Table 2).

4. Datasets

We demonstrate the broad applicability of our approach by validating it on domains with different signal and noise structure: natural videos, fluorescence microscopy, and electron microscopy.

Natural videos. We perform controlled experiments on natural videos by adding iid Gaussian noise to the DAVIS dataset [27], which contains clean videos of resolution 854x480. The training/validation/test split is 60/30/30 videos, respectively. We use an additional independent dataset for validation, Set8 [32], composed of 4 color videos from the Derfs Test Media collection and 4 color videos captured with a GoPro camera.

Fluorescence microscopy. We apply our approach to fluorescence-microscopy recordings of live cells from the cell-tracking challenge in [34]. We use two videos: Fluo-C2DL-MSC (CTC-MSC) depicting mesenchymal stem cells, and Fluo-N2DH-GOWT1 (CTC-N2DH) depicting GOWT1 cells. This dataset illustrates the challenges of applying supervised approaches to real data: there is no ground-truth clean data, and the noise model is unknown.

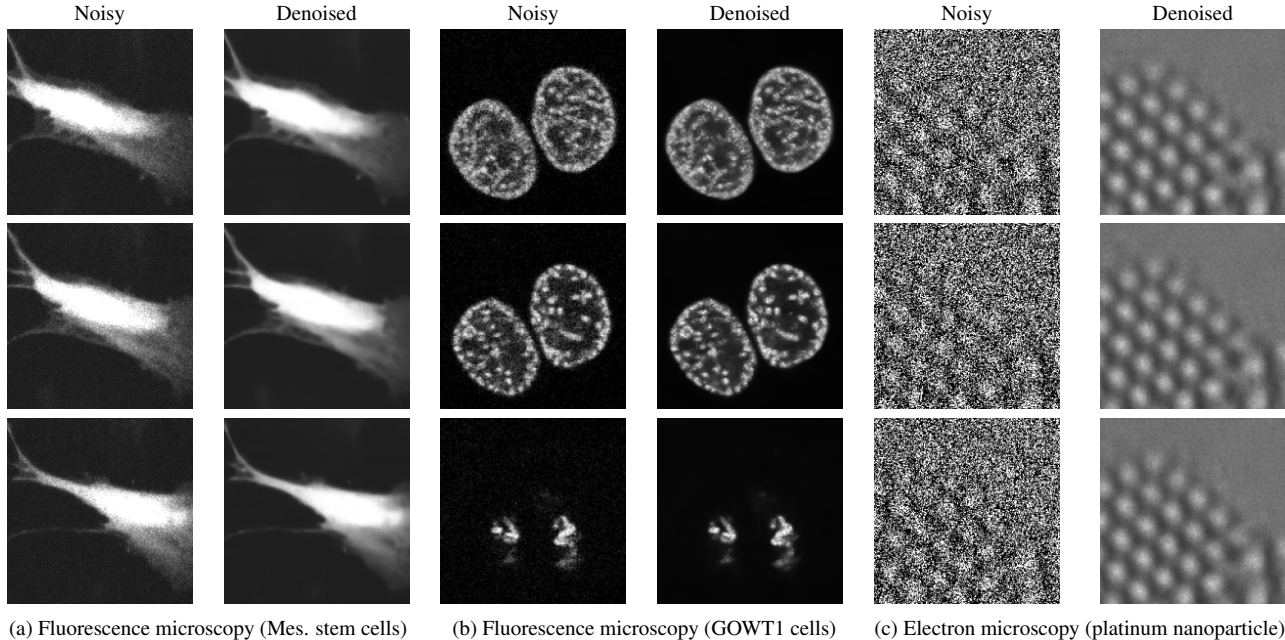
Electron microscopy. We also apply our methodology

to a transmission electron microscopy dataset from [26]. The data consist of a 40-frame video depicting a platinum nanoparticle supported on a cerium oxide base. The noise follows Poisson statistics. The average image intensity is 0.45 electrons/pixel, which results in an extremely low signal-to-noise ratio (a large fraction of pixels do not contain any electrons!). As with the fluorescence-microscopy data, no ground-truth clean images are available.

5. Experiments

Natural videos. We train UDVD on the DAVIS training set (see Section A.3 for details on the training procedure). Following the methodology of previous works in supervised and unsupervised image and video denoising, we add iid Gaussian noise with standard deviation $\sigma = 30$ on the clean videos during training. Evaluation is carried out on the DAVIS test set and on Set8 by comparing to the clean ground-truth videos via PSNR and SSIM [35]. We test the network at different noise levels and frame rates to evaluate its robustness (see Section E). In addition, we perform an ablation study to compare versions of UDVD that use different numbers of noisy frames to estimate each denoised frame. Finally, to recreate a more realistic unsupervised setting, we also train and test UDVD on four individual videos with a single noise realization.

Real-world data. We train UDVD on the fluorescence-microscopy data described in Section 4 following the same procedure as for the natural videos, including data augmentation. In the case of the electron-microscopy data, as reported in [26], training without early stopping results in severe overfitting. We therefore trained on the first 35 frames of the video, and used the remaining 5 as a validation set to perform early stopping based on mean-squared error.



(a) Fluorescence microscopy (Mes. stem cells) (b) Fluorescence microscopy (GOWT1 cells) (c) Electron microscopy (platinum nanoparticle)

Figure 3. **Denoising real-world microscopy data.** Results from applying UDVD to the fluorescence-microscopy and the electron-microscopy video described in Section 4. Qualitatively, UDVD succeeds in removing noise while preserving the underlying signal structure, even for the highly noisy electron-microscopy data. See our [website](#) for denoised videos.

6. Results

Comparison with other approaches on natural videos.

We compare the performance of UDVD with several popular methods (see Section 2): Bayesian processing of spatiotemporal patches (VNLB [19]), an extension of the popular image-denoising algorithm BM3D [7] (VBM4D [23]), supervised deep-learning methods (VNLnet [8], DVDnet [31], FastDVDnet [32]). As shown in Table 1, UDVD achieves comparable performance to the supervised state-of-the-art on the DAVIS test set and slightly outperforms these methods on Set8 at multiple noise levels. It also outperforms unsupervised techniques such as VNLB and VBM4D. Examples are shown in Figure 1.

Use of temporal information. UDVD estimates each frame from k surrounding contiguous frames. To validate the effect of using more temporal information, we tested $k \in \{1, 3, 5\}$. As shown in Table 1, performance improves substantially and monotonically with k (see Section B for validation on more noise levels and visual comparisons). This is consistent with the literature on supervised learning [32]. The performance gains arising from operating on a longer-duration temporal interval are more substantial at higher noise levels. Analysis of UDVD shows that the network tends to ignore temporally distant frames at lower noise levels (see Fig 4 and Section F).

Generalization across noise levels. UDVD generalizes strongly across noise levels not encountered during training. The results in Table 1 are obtained with a network trained

only at a fixed noise level of $\sigma = 30$. This generalization ability is consistent with previous bias-free networks for image denoising [25]. See Section E for additional discussion and results.

Unsupervised denoising from limited data. In order to validate our approach on a more challenging setting that is closer to the practical applications of unsupervised denoising, we trained and tested UDVD on four individual videos. As shown in Table 2, when combined with data augmentation, this version of UDVD achieves comparable results to the version trained on the DAVIS dataset, even though the DAVIS dataset is 80 times larger (60 videos, with 4219 total frames) and includes different realizations of the added noise.

Real-world microscopy data. UDVD is able to effectively denoise the fluorescence-microscopy and the electron-microscopy datasets described in Section 4. This can be appreciated qualitatively in Figure 3 and the videos (see our [website](#)).

7. Automatic Motion Compensation

Most previous approaches for video denoising rely on explicit motion compensation [22, 1, 3, 23]. This requires estimating the optical flow, which is the local translational motion of features in the image arising from the motion of objects and surfaces in a visual scene relative to the camera. Several CNN-based denoisers build motion estimation into the architecture [31, 38]. In particular, motion compensa-

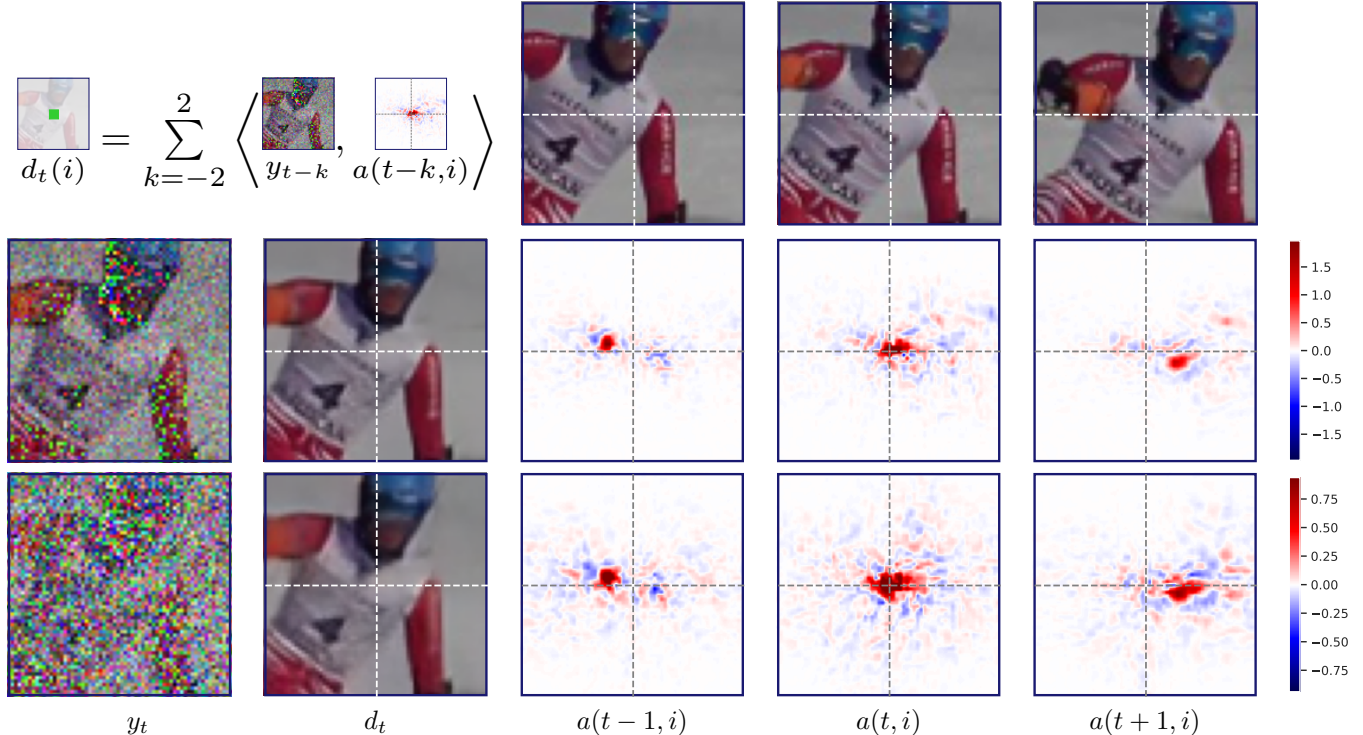


Figure 4. **Video denoising as spatiotemporal adaptive filtering.** Visualization of the linear weighting functions ($a(k, i)$, Eq. 2) of UDVD. The left two columns show the noisy frame y_t at two levels of noise, and the corresponding denoised frame, d_t . Weighting functions $a(k, i)$ corresponding to the pixel i (at the intersection of the dashed white lines), for three successive frames, are shown in the last three columns. The weighting functions adapt to underlying image content, and are shifted to track the motion of the skier. As the noise level σ increases, their spatial extent grows, averaging out more of the noise while respecting object boundaries. The weighting functions corresponding to the five frames approximately sum to one, and thus compute a local average (although some weights are negative, depicted in blue) (Fig 8). See Fig 9, 10, 11, and 12 for additional examples using UDVD and Fig 13 for additional examples using FastDVDnet [32]

tion is critical to the Frame2frame framework for unsupervised denoising, which uses motion compensation to register contiguous images [10, 11]. In contrast, recent supervised video denoising networks like FastDVDnet [32] and ViDeNN [6], as well as our unsupervised UDVD, do not perform any explicit motion compensation. Despite this, they achieve state-of-the-art results. The empirical performance of these approaches suggests that the networks must somehow be exploiting temporal information successfully. Here, we study this phenomenon through an analysis of the denoising mapping, which reveals that these networks do perform implicit motion compensation.

Gradient-based analysis. We build upon the approach of [25] to study CNNs trained for image denoising. Let $y \in \mathbb{R}^{nT}$ be a flattened video sequence containing T noisy frames with n pixels each, processed by a CNN. We define the denoising function $f_i : \mathbb{R}^{nT} \rightarrow \mathbb{R}$ as the map between the noisy video and the denoised value $d_i := f_i(y)$ of the CNN output at the i^{th} pixel. A first-order Taylor approximation of the denoising function may be written as:

$$d_i := f_i(y) = \langle \nabla f_i(y), y \rangle + b, \quad (1)$$

where $\nabla f_i(y) \in \mathbb{R}^{nT}$ denotes the gradient of f_i at y . The constant $b := f_i(y) - \langle \nabla f_i(y), y \rangle$ is the net bias of the network, a combined function of all additive constants in the convolutional and batch-normalization layers of the CNN. In [25], it was shown that the equivalent bias tends to be negligible for CNNs trained to denoise natural images corrupted by additive Gaussian noise, but is a primary cause of failures to generalize to noise levels not encountered during training. The authors find that removing all additive constants to make the CNN architecture *bias-free* enables generalization far beyond the noise levels used to train the network, and also allows analysis and interpretation of the denoising function by visualization of the gradient.

In our proposed architecture, we use bias-free networks for all CNN modules. As such, the denoised value at the i^{th} pixel may be written

$$d(i) = \langle \nabla f_i(y), y \rangle = \sum_{k=1}^T \langle a(k, i), y_k \rangle, \quad (2)$$

where y_k denotes each of the T flattened frames that compose the noisy video, and $a(k, i)$ is the corresponding por-

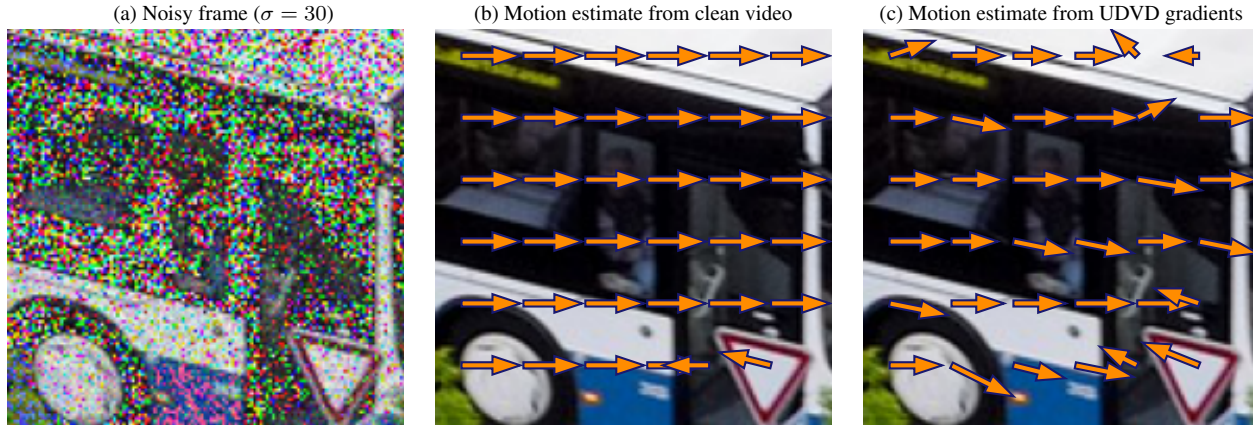


Figure 5. **CNNs trained for denoising automatically learn to perform motion estimation.** (a) Noisy frame from a video in the DAVIS dataset. (b) Optical flow direction at multiple locations of the image obtained using a state-of-the-art algorithm applied to the *clean video*. (c) Optical flow direction estimated from the shift of the adaptive filter obtained by differentiating the network, which is trained exclusively with noisy videos and no optical flow information. Optical flow estimates are well-matched to those in (b), but deviate according to the aperture problem at oriented features (ess black vertical edge of bus door), and in homogeneous regions (see bus roof, top right). See Fig 15, 16, 17 and 18 for additional examples using UDVD and FastDVDnet.

tion of the gradient of f_i at y . Each vector $a(k, i)$ can be interpreted as an *equivalent filter* that produces an estimate of the denoised video at pixel i by performing a weighted average of the noisy observations over space and time.

Visualizing these equivalent filters reveals that the UDVD network learns to denoise by performing averaging over an adaptive spatiotemporal neighborhood of each pixel. As illustrated in Figure 4 (and in additional examples in Section F), when the noise level increases, the averaging is carried out over larger regions. This intuitive behavior is also seen in classical linear Wiener filters [37], which are larger for higher levels of noise. The crucial difference is that in the case of CNNs, the equivalent filters are *adaptive*: they respect object boundaries in time and space, and take into account their motion. This is apparent in Figure 4. The equivalent filters in adjoining frames are automatically shifted spatially to compensate for the movement of the skier (additional examples are provided in Section F). This is not unique to UDVD: CNNs trained in a supervised fashion have the same property (also shown in Section F).

Optical-flow estimation. In order to validate our observation that CNNs exclusively trained for denoising are able to detect and exploit video motion, we use the equivalent filters of the networks to estimate the optical flow. To estimate the optical flow from the t^{th} frame to the $(t+1)^{\text{th}}$ frame at the i^{th} pixel, we compute the difference between the position of the centroid of the equivalent filter corresponding to the pixel at times t , $a(t, i)$, and time $t+1$, $a(t+1, i)$. To increase the stability of the estimated flow, we compute the filter centroid through a robust weighted average that only includes entries with relatively large values (within 20% of maximum value in the filter).

The optical-flow estimates obtained from the gradients of the trained UDVD network are surprisingly precise, even at very high noise levels. Figure 5, and additional figures in Section F, show that the results are similar to those obtained by applying an algorithm for optical-flow estimation (DeepFlow [36]) on the corresponding *clean video*. This demonstrates that the CNNs are able to implicitly estimate motion from data, despite the fact that they were not trained on that problem, and *even in the presence of substantial noise corruption*, a setting that is quite challenging for optical-flow estimation techniques. We also observe that the optical-flow estimates obtained from UDVD gradients tend to be less accurate for pixels near strongly oriented features or in highly homogeneous regions, where the local motion is ambiguous. In these regions, the local motion is underconstrained. Local optical flow estimation techniques typically resolve this by incorporating additional constraints (e.g., smoothness) on the motion field). The adaptive filters in a video denoiser need only compute averages that are good for denoising. In the case of oriented content, they appear to exploit the well-known “aperture problem”, broadly integrating along the oriented contours in successive frames. In the case of blank regions, they integrate more homogeneously over surrounding pixels to achieve good denoising.

8. Conclusion

In this work we propose a method for unsupervised deep video denoising that achieves comparable performance to state-of-the-art supervised approaches. Combined with data-augmentation techniques, the method achieves effective denoising even when trained exclusively on short in-

dividual noisy sequences, which enables its application to real-world microscopy data. An important topic for future research is performing quantitative validation on such data (either through careful simulation, or acquisition at multiple SNRs). In addition, we perform a gradient-based analysis of denoising CNNs, which reveals that they learn to perform implicit adaptive motion compensation. This suggests several interesting research directions. For example, denoising may be a useful pretraining task for optical-flow estimation or other computer-vision tasks requiring motion estimation.

Acknowledgements

We gratefully acknowledge financial support from the National Science Foundation (NSF). NSF NRT HDR Award 1922658 partially supported SM who designed, implemented and analyzed the proposed methodology. NSF CBET 1604971 supported JLV and PAC and NSF OAC-1940263 supported RM and PAC who acquired and processed the electron-microscope experimental data. NSF OAC-1940097 supported CFG who supervised the design, implementation and analysis of the methodology. All authors participated in writing and reviewing the manuscript.

References

- [1] Pablo Arias and Jean-Michel Morel. Video denoising via empirical bayesian estimation of space-time patches. *Journal of Mathematical Imaging and Vision*, 60(1):70–93, 2018. 1, 2, 6
- [2] Joshua Batson and Loic Royer. Noise2self: Blind denoising by self-supervision. In *Proceedings of the 36th International Conference on Machine Learning*, pages 524–533, 2019. 1, 4
- [3] Antoni Buades, Jose-Luis Lisani, and Marko Miladinović. Patch-based video denoising with optical flow estimation. *IEEE Transactions on Image Processing*, 25(6):2573–2586, 2016. 1, 2, 6
- [4] S Grace Chang, Bin Yu, and Martin Vetterli. Adaptive wavelet thresholding for image denoising and compression. *IEEE Trans. Image Processing*, 9(9):1532–1546, 2000. 2
- [5] Yunjin Chen and Thomas Pock. Trainable nonlinear reaction diffusion: A flexible framework for fast and effective image restoration. *IEEE transactions on pattern analysis and machine intelligence*, 39(6):1256–1272, 2016. 2
- [6] Michele Claus and Jan van Gemert. Videnn: Deep blind video denoising. In *Proceedings of the IEEE/CVF Conference on Computer Vision and Pattern Recognition Workshop*, pages 1843–1852, 2019. 2, 4, 7
- [7] Kostadin Dabov, Alessandro Foi, Vladimir Katkovnik, and Karen Egiazarian. Image denoising by sparse 3-d transform-domain collaborative filtering. *IEEE Transactions on Image Processing*, pages 2080–2095, 2017. 2, 6
- [8] Axel Davy, Thibaud Ehret, Jean-Michel Morel, Pablo Arias, and Gabriele Facciolo. A non-local cnn for video denoising. In *2019 IEEE International Conference on Image Processing (ICIP)*, pages 2409–2413. IEEE, 2019. 2, 6
- [9] Valéry Dewila, Jérémy Anger, Axel Davy, Thibaud Ehret, Pablo Arias, and Gabriele Facciolo. Self-supervised training for blind multi-frame video denoising. *arXiv preprint arXiv:2004.06957*, 2020. 3
- [10] Thibaud Ehret, Axel Davy, Jean-Michel Morel, Gabriele Facciolo, and Pablo Arias. Model-blind video denoising via frame-to-frame training. In *Proceedings of the IEEE/CVF Conference on Computer Vision and Pattern Recognition*, pages 11361–11370, 2019. 1, 2, 3, 7
- [11] Bichuan Guo, Jiangtao Wen, Zhen Xia, Shan Liu, and Yuxing Han. Learning model-blind temporal denoisers without ground truths. *arXiv preprint arXiv:2007.03241*, 2020. 1, 3, 7
- [12] Shi Guo, Zifei Yan, Kai Zhang, Wangmeng Zuo, and Lei Zhang. Toward convolutional blind denoising of real photographs. In *Proceedings of the IEEE/CVF Conference on Computer Vision and Pattern Recognition*, pages 1712–1722, 2019. 2
- [13] Sergey Ioffe and Christian Szegedy. Batch normalization: Accelerating deep network training by reducing internal covariate shift. *arXiv preprint arXiv:1502.03167*, 2015. 11, 14
- [14] Wesley Khademi, Sonia Rao, Clare Minnerath, Guy Hagen, and Jonathan Ventura. Self-supervised poisson-gaussian denoising. *arXiv preprint arXiv:2002.09558*, 2020. 4
- [15] Diederik P Kingma and Jimmy Ba. Adam: A method for stochastic optimization. *arXiv preprint arXiv:1412.6980*, 2014. 12
- [16] Alexander Krull, Tim-Oliver Buchholz, and Florian Jug. Noise2void - learning denoising from single noisy images. In *Proceedings of the IEEE/CVF Conference on Computer Vision and Pattern Recognition*, pages 2124–2132, 2019. 1, 4
- [17] Alexander Krull, Tomas Vicar, and Florian Jug. Probabilistic noise2void: Unsupervised content-aware denoising. *arXiv preprint arXiv:1906.00651*, 2019. 4
- [18] Samuli Laine, Tero Karras, Jaakko Lehtinen, and Timo Aila. High-quality self-supervised deep image denoising. In *Advances in Neural Information Processing Systems 32*, pages 6970–6980, 2019. 1, 2, 4, 11, 12
- [19] Marc Lebrun, Antoni Buades, and Jean-Michel Morel. A nonlocal bayesian image denoising algorithm. *SIAM Journal on Imaging Sciences*, 6(3):1665–1688, 2013. 2, 6
- [20] Yann LeCun, Yoshua Bengio, and Geoffrey Hinton. Deep learning. *nature*, 521(7553):436, 2015. 1, 2
- [21] Jaakko Lehtinen, Jacob Munkberg, Jon Hasselgren, Samuli Laine, Tero Karras, Miika Aittala, and Timo Aila. Noise2noise: Learning image restoration without clean data. In *Proceedings of the 35th International Conference on Machine Learning*, pages 2965–2974, 2018. 1, 3
- [22] Ce Liu and William T Freeman. A high-quality video denoising algorithm based on reliable motion estimation. In *European conference on computer vision*, pages 706–719. Springer, 2010. 1, 2, 6
- [23] Matteo Maggioni, Giacomo Boracchi, Alessandro Foi, and Karen Egiazarian. Video denoising, deblocking, and enhancement through separable 4-d nonlocal spatiotempo-

- ral transforms. *IEEE Transactions on image processing*, 21(9):3952–3966, 2012. 1, 2, 6
- [24] Peyman Milanfar. A tour of modern image filtering: New insights and methods, both practical and theoretical. *IEEE signal processing magazine*, 30(1):106–128, 2012. 2
- [25] Sreyas Mohan, Zahra Kadkhodaie, Eero P. Simoncelli, and Carlos Fernandez-Granda. Robust and interpretable blind image denoising via bias-free convolutional neural networks. In *Proceedings of the International Conference on Learning Representations*, 2020. 4, 6, 7, 12, 13
- [26] Sreyas Mohan, Ramon Manzorro, Joshua L Vincent, Binh Tang, Dev Yashpal Sheth, Eero P Simoncelli, David S Matetson, Peter A Crozier, and Carlos Fernandez-Granda. Deep denoising for scientific discovery: A case study in electron microscopy. *arXiv preprint arXiv:2010.12970*, 2020. 5
- [27] Jordi Pont-Tuset, Federico Perazzi, Sergi Caelles, Pablo Arbeláez, Alex Sorkine-Hornung, and Luc Van Gool. The 2017 davis challenge on video object segmentation. *arXiv preprint arXiv:1704.00675*, 2017. 5
- [28] Javier Portilla, Vasily Strela, Martin J Wainwright, and Eero P Simoncelli. Image denoising using scale mixtures of gaussians in the wavelet domain. *IEEE Trans. Image Processing*, 12(11), 2003. 2
- [29] Mangal Prakash, Manan Lalit, Pavel Tomancak, Alexander Krull, and Florian Jug. Fully unsupervised probabilistic noise2void. *arXiv preprint arXiv:1911.12291*, 2019. 4
- [30] Olaf Ronneberger, Philipp Fischer, and Thomas Brox. U-net: Convolutional networks for biomedical image segmentation. In *International Conference on Medical image computing and computer-assisted intervention*, pages 234–241. Springer, 2015. 2, 4, 11
- [31] Matias Tassano, Julie Delon, and Thomas Veit. Dvdnet: A fast network for deep video denoising. In *Proceedings of the IEEE International Conference on Image Processing*, pages 1805–1809, 2020. 1, 2, 4, 6, 12, 13
- [32] Matias Tassano, Julie Delon, and Thomas Veit. Fastdvdnet: Towards real-time deep video denoising without flow estimation. In *Proceedings of the IEEE/CVF Conference on Computer Vision and Pattern Recognition*, pages 1351–1360, 2020. 1, 2, 4, 5, 6, 7, 12, 13
- [33] Carlo Tomasi and Roberto Manduchi. Bilateral filtering for gray and color images. In *ICCV*, volume 98, 1998. 2
- [34] Vladimír Ulman et al. An objective comparison of cell-tracking algorithms. *Nature Methods*, 14:1141–1152, 2017. 5
- [35] Zhou Wang, Alan C Bovik, Hamid R Sheikh, Eero P Simoncelli, et al. Image quality assessment: from error visibility to structural similarity. *IEEE Trans. Image Processing*, 13(4):600–612, 2004. 2, 5
- [36] Philippe Weinzaepfel, Jerome Revaud, Zaid Harchaoui, and Cordelia Schmid. Deepflow: Large displacement optical flow with deep matching. In *Proceedings of the IEEE international conference on computer vision*, pages 1385–1392, 2013. 2, 8, 15
- [37] Norbert Wiener. *Extrapolation, interpolation, and smoothing of stationary time series: with engineering applications*. Technology Press, 1950. 8
- [38] Tianfan Xue, Baian Chen, Jiajun Wu, Donglai Wei, and William T Freeman. Video enhancement with task-oriented flow. *International Journal of Computer Vision (IJCV)*, 127(8):1106–1125, 2019. 1, 2, 6
- [39] Songhyun Yu, Bumjun Park, Junwoo Park, and Jechang Jeong. Joint learning of blind video denoising and optical flow estimation. In *Proceedings of the IEEE/CVF Conference on Computer Vision and Pattern Recognition (CVPR) Workshops*, June 2020. 1, 3
- [40] H. Yue, C. Cao, L. Liao, R. Chu, and J. Yang. Supervised raw video denoising with a benchmark dataset on dynamic scenes. In *2020 IEEE/CVF Conference on Computer Vision and Pattern Recognition (CVPR)*, pages 2298–2307, 2020. 2, 3
- [41] Christopher Zach, Thomas Pock, and Horst Bischof. A duality based approach for realtime tv-l 1 optical flow. In *Joint pattern recognition symposium*, pages 214–223. Springer, 2007. 3
- [42] Kai Zhang, Wangmeng Zuo, Yunjin Chen, Deyu Meng, and Lei Zhang. Beyond a gaussian denoiser: Residual learning of deep cnn for image denoising. *IEEE Transactions on Image Processing*, pages 3142–3155, 2017. 2, 12, 13

A. Implementation Details of Unsupervised Deep Video Denoising

A.1. Restricting the Field of View

In UDVD, we rotate the input frames by multiples of 90° and process them through four separate branches (with shared parameters) containing asymmetric convolutional filters that are *vertically causal*. As a result, the branches produce outputs that only depend on the pixels above (0° rotation), to the left (90°), below (180°) or to the right (270°) of the output pixel. We use a UNet [30] style architecture for each branch of UDVD. The field of view of the UNet is constrained by restricting the field of view of the convolutional, downsampling and upsampling layers that are used to build the UNet.

Convolutional Layers: We restrict the receptive field of each convolutional layer to extend only upwards following the strategy proposed in [18]. Let the filter size be $h \times w$. We zero-pad the top region of the input tensor with $k = \lfloor h/2 \rfloor$ zero rows before convolution and remove the bottom k rows after convolution. This is equivalent to convolving with a filter, where all weights below the center row are zero, so that the field of view only extends upwards.

Downsampling and Upsampling Layers: Following [18] we restrict the receptive field of the downsampling layer by creating an offset of one pixel (zero-pad with a row of zeros on the top and remove a row of pixels from below) before performing max-pooling using a 2×2 kernel. This operation restricts the field of view of the downsampling and upsampling operation pair.

Note that we do not use BatchNorm [13] layers in UDVD as computing the spatial mean and variance would modify the field of view to include the center pixel.

A.2. Adding the Noisy Pixel Back

The denoised generated by the proposed architecture at each pixel is computed without using the noisy observation at that location. This avoids overfitting – i.e. learning the trivial identity map that minimizes the mean-squared error cost function – but ignores important information provided by the noisy pixel. In the case of Gaussian additive noise, we can use this information via a precision-weighted average between the network output and the noisy pixel value. Following [18], the weights in the average are derived by assuming a Gaussian distribution for the error in the blind-spot estimates of the (color) pixel values. The CNN architecture is trained to estimate the mean and covariance of this distribution at each pixel by maximizing the log likelihood of the noisy data. We explain this in detail in the following paragraphs.

UDVD estimates the value of a pixel based on the noisy pixels in its neighbourhood. We model the distribution of the three color channels of a pixel $x \in \mathcal{R}^3$ given the noisy neighbourhood Ω_y as $p(x|\Omega_y) = \mathcal{N}(\mu_x, \Sigma_x)$, where $\mu_x \in \mathcal{R}^3$ and $\Sigma_x \in \mathcal{R}^3$ represent the mean vector and covariance matrix. Let $y = x + \eta$, $\eta \sim \mathcal{N}(0, \sigma^2 I_3)$ be the observed noisy pixel. We integrate the information in the noisy pixel with the UDVD output by computing the mean of the posterior $p(x|y, \Omega_y)$, given by

$$E[x|y] = (\Sigma_x^{-1} + \sigma^{-2}I)^{-1}(\Sigma_x^{-1}\mu_x + \sigma^{-2}y). \quad (3)$$

Note that the posterior mean has a very intuitive interpretation. When the signal variance is high compared to noise variance (i.e. the uncertainty in our estimation is high) the posterior mean favours noisy pixel value. We estimate μ_x and Σ_x as a function of the neighbourhood Ω_y using the network architecture discussed earlier. If x is a grayscale image, then the output of the network consists of two channels - one for μ_x and one for σ_x . When the input image has k channels, the output consists of k channels for μ_x and $k(k-1)/2$ for the upper-triangular entries of Σ_x .

One can estimate μ_x and Σ_x directly from the noisy data by maximizing the likelihood. Using our distributional assumptions, the noisy pixels y follows a Gaussian distribution, $y \sim \mathcal{N}(\mu_y, \Sigma_y)$, where $\mu_y = \mu_x$ and $\Sigma_y = \Sigma_x + \sigma^2 I$. Therefore, the loss function or the negative log likelihood is:

$$\mathcal{L}(\mu_x, \Sigma_x) = \frac{1}{2}[(y - \mu_x)^T (\Sigma_x + \sigma^2 I)^{-1} (y - \mu_x)] + \frac{1}{2} \log |\Sigma_x + \sigma^2 I|. \quad (4)$$

If σ is unknown during training and has to be estimated, we use a separate neural network with the same architecture to do so. In such cases, we add a small regularization term equal to -0.1σ for numerical stability, following [18].

For the experiments with real data, the noise distribution is unknown, so we simply ignore the central pixel.

A.3. Architecture and Training

Architecture: The overall architecture is explained in Section 3 of the paper. The network architecture for the D1 and D2 blocks is described in Table 3. D1 has $k_1 = 9$ input channels and $k_2 = 32$ output channels. D2 has $k_1 = 96$ input channels

Name	N_{out}	Function
Input	k_1	
enc_conv_0	48	Convolution 3×3
enc_conv_1	48	Convolution 3×3
enc_conv_2	48	Convolution 3×3
pool_1	48	MaxPool 2×2
enc_conv_3	48	Convolution 3×3
enc_conv_4	48	Convolution 3×3
enc_conv_5	48	Convolution 3×3
pool_2	48	MaxPool 2×2
enc_conv_6	96	Convolution 3×3
enc_conv_7	96	Convolution 3×3
enc_conv_8	48	Convolution 3×3
upsample_1	48	NearestUpsample 2×2
concat_1	96	Concatenate output of pool_1
dec_conv_0	96	Convolution 3×3
dec_conv_1	96	Convolution 3×3
dec_conv_2	96	Convolution 3×3
dec_conv_3	96	Convolution 3×3
upsample_2	96	NearestUpsample 2×2
concat_2	$96+k_1$	Concatenate output of Input
dec_conv_4	96	Convolution 3×3
dec_conv_5	96	Convolution 3×3
dec_conv_6	96	Convolution 3×3
dec_conv_7	k_2	Convolution 3×3

Table 3. **Network architecture used for UDVD.** The convolution and pooling layers are the blind-spot variants described in Section A.1. k_1 and k_2 represent the number of input and output channels of the base network respectively.

and $k_2 = 96$ output channels. The architecture of D1 and D2 are analogous to the blocks in FastDVDnet [32] to facilitate fair comparison with the supervised models. As described in Fig. 2 of the paper, D2 is followed by a derotation and the output is passed to a series of three cascaded 1×1 convolutions and non-linearity for reconstruction with 4 and 96 intermediate output channels, as in [18]. The final convolutional layer is linear and has 9 output channels, 3 representing the RGB value of the denoised image and 6 representing its covariance matrix. We use the same architecture for fluorescence microscopy and electron microscopy with the number of input channels to UDVD modified to 5 and number of output channels modified to 1.

Training Details: Following the convention in image and video denoising, we train UDVD on 128×128 patches extracted from our dataset [42, 25, 18, 32, 31] (this is also consistent with the training methodology of the supervised baselines). For the natural video and fluorescence microscopy datasets, no data augmentation was applied. For electron microscopy dataset, we applied spatial flipping, time reversal and time subsampling (i.e. skipping frames).

Optimization Details: All networks were trained using Adam [15] optimizer with a starting learning of 10^{-4} . The learning rate was decreased by a factor of 2 at checkpoints [20, 25, 30] during a total training of 40 epochs. We did not experiment with other learning rate schedules such as cosine scheduling, which is a popular choice in unsupervised image denoising [18].

B. Ablation Study on Number of Input Frames

We perform an ablation study on the number of frames k UDVD uses as input, $k \in \{1, 3, 5\}$. UDVD with $k = 1$ is equivalent to the blind-spot network proposed for image denoising in [18]. In this section we describe the architectural and training details for UDVD with $k \in \{1, 3, 5\}$ and present some additional results.

σ	DAVIS				Set8			
	Supervised CNN	Unsupervised CNN (UDVD)			Supervised CNN	Unsupervised CNN (UDVD)		
	5 frames	1 frame	3 frames	5 frames	5 frames	1 frame	3 frames	5 frames
20	35.86	33.98	34.75	34.99	33.37	32.20	32.97	33.25
30	34.06	32.79	33.42	33.86	31.60	30.68	31.46	31.86
40	32.80	31.47	32.15	32.61	30.37	29.33	30.18	30.62
50	31.83	30.46	31.15	31.63	29.42	28.28	29.18	29.63
60	30.97	29.63	30.33	30.84	28.75	27.44	28.36	28.82
70	30.16	28.94	29.64	30.16	28.00	26.75	27.66	28.14
80	29.20	28.35	29.05	29.58	27.20	26.16	27.06	27.55

Table 4. **Performance of UDVD.** Table shows the mean PSNR values of a state-of-the-art supervised video denoiser (FastDVDnet [32]) and UDVD with the denoised frame being predicted from $k \in \{1, 3, 5\}$ surrounding frames. The performance of UDVD monotonically increases with k and is comparable for supervised denoising across all noise levels. All the three UDVD networks reported here are trained for only $\sigma = 30$. FastDVDnet is trained for $\sigma \in [5, 55]$.

Architectural Details: UDVD with $k = 1$ contains only one UNet style network in each branch with architecture described in Table 3 and Section A.3. There are 3 input channels and 9 output channels (3 for the RGB channels in each denoised pixel and 6 for the corresponding covariance matrix). UDVD with $k = 3$ has a similar architecture as for $k = 1$ but has 9 input channels instead (3 channels for each frame). The architecture for $k = 5$ is described in Section A.3.

Training Details: UDVD with $k \in \{1, 3, 5\}$ was trained on the DAVIS dataset with $\sigma = 30$. The training details were as described in Section A.3.

Results: As shown in Table 1 of the paper and Table 4 performance improves substantially and monotonically with k (the number of surrounding frames used to denoise each frame) across a wide range of noise levels. This difference in performance can also be observed visually. Fig 6 shows an example where the texture details of the brick wall and the fence are not well recovered when using only a single noisy frame. The texture is estimated better when using 5 noisy frames to predict the denoised output.

C. Denoising Results on Natural Video Datasets

In this section we provide additional comparisons between UDVD and supervised CNN-based methods.

1. Table 4 shows the performance of UDVD trained at $\sigma = 30$, and FastDVDnet trained for $\sigma \in [5, 55]$ when evaluated on the DAVIS test set and Set8 corrupted with $\sigma \in \{20, 40, \dots, 80\}$. UDVD achieves comparable performance to FastDVDnet on DAVIS test set and slightly outperforms it on Set8 at all noise levels.
2. Examples of noisy videos, and denoised counterparts obtained using UDVD can be found on our [website](#).

D. Denoising Results on Microscopy Video Datasets

The noisy fluorescence microscopy and electron microscopy data, and the denoised videos obtained with UDVD can be found on our [website](#).

E. Generalization Across Noise and Frame Rate

Ideally, a denoiser should be able to denoise videos corrupted at a wide range of noise levels. This is usually achieved by training the CNN on examples corrupted with a range of noise strength [42, 32, 31]. The range of noise levels on which the network is trained is called the *training range* of the network.

Generalization outside the training range: The authors of [25] showed that CNNs trained for image denoising generalize well on test images corrupted with noise in the training range, but fails catastrophically when corrupted with noise strength



Figure 6. **Comparison of blind image and video denoising.** Example from the DAVIS dataset. (a) Ground truth frame. (b) Noisy frame. (c) Reconstruction using a single frame. The texture details of the brick wall and the fence are not recovered well. Reconstruction using (d) 3 and (e) 5 surrounding frames produces an improved texture estimate.

outside the training range. The authors provided evidence that the overfitting is due to additive terms in the convolutional layers (and BatchNorm [13]) and showed that a CNN with no additive terms, called a *bias-free* CNN generalizes well outside the training range. UDVD uses a bias-free architecture and generalizes well to noise levels outside its training range (Fig 7).

Generalization across frame rates: To test generalization across frame rates, we simulated faster videos by skipping frames of videos in Set8. Fig 7 shows that UDVD generalizes robustly to faster videos and maintains a significant gain in performance over single-image denoising even when tested on videos where a large number of frames have been skipped (i.e. at a very low frame rate).

F. Analysis of CNN-based Video Denoising

F.1. Natural Videos

In Section 7 and Fig 4 of the paper we examined the equivalent filters and illustrated that UDVD learns to denoise by performing an average over a spatiotemporal neighbourhood of each pixel. Here we examine equivalent filters for more videos and a supervised CNN (FastDVDnet) and show that similar observations hold.

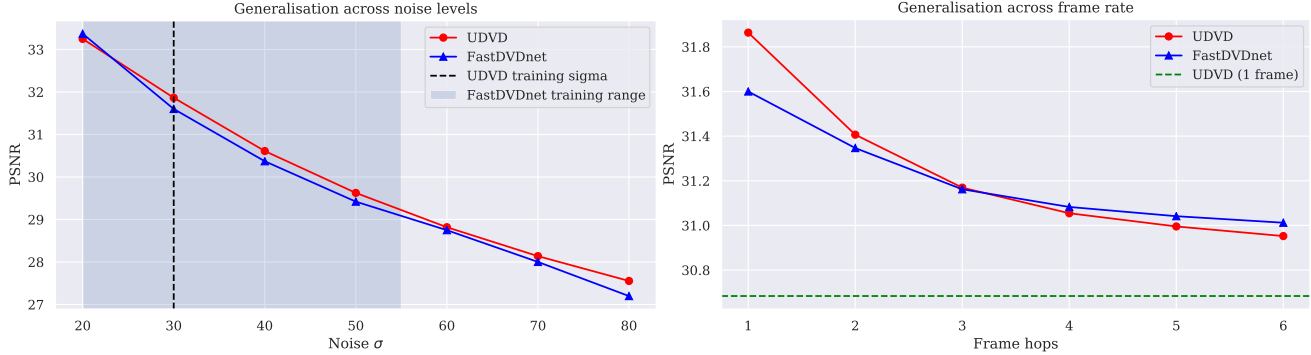


Figure 7. **Generalization across noise levels and frame rates.** (left) UDVD trained at only $\sigma = 30$ generalizes well to noise levels not seen during training. The plotted points represent mean PSNR values evaluated on Set8. (right) UDVD generalizes well to faster videos (created by skipping frames) and consistently outperforms a baseline image denoiser (UDVD with a single input frame, shown as a green dashed line).

Adaptive filtering: Fig 9, 10, 11 and 12 shows filters computed at a pixel for 4 different videos at 4 different noise levels. The filters adapt to the underlying signal content. They span larger areas as the noise level increases. These observations also holds for FastDVDnet, which is trained with supervision (Fig 13)

Contribution of neighbouring frames for denoising: UDVD tends to ignore temporally distant frames at lower noise levels as shown in Fig 9, 10, 11 and 12. This phenomenon is quantified in Fig 8 by plotting the contribution of each frame to the denoised pixel by averaging over **5000** pixels from **250** random patches of size 128×128 . At higher noise levels, UDVD seems to use distant frames more. This is consistent with the ablation study, which shows that for higher noise levels using more surrounding frames improves the denoising performance. Similar results hold for supervised CNN FastDVDnet, as shown in Fig 13.

Local Averaging: The weighting functions or equivalent filters perform an approximate averaging operation. They are mostly non-negative (although they do have some negative entries as depicted in blue in Fig 9, 10, 11 and 12) and they approximately sum up to one (see Fig 8).

F.2. Microscopy Data

Equivalent filters for the fluorescence-microscopy and the electron-microscopy data are shown in Fig 14. The fluorescence-microscopy data have a low noise level. As expected from the results on natural videos (see Section C), the weighting functions are mostly confined to the middle frame (as quantified in Fig 8). In the electron-microscopy dataset the weighting functions shows that the network relies on adjacent frames to estimate the denoised (as quantified in Fig 8).

F.3. Motion Estimation

Figures 9, 10, 11 and 12 show that the equivalent filters in adjoining frames are automatically shifted spatially to account for the movement of objects in the videos. We extracted motion information using the shift as explained in Section 7. Figures 15, 16, 17 and 18 show additional examples for UDVD and FastDVDnet. The estimated optical flow is mostly consistent with the estimated obtained by DeepFlow [36] applied on the clean videos. The motion estimates obtained from the equivalent filters tends to be less accurate for pixels near strongly correlated features or highly homogeneous regions where the local motion is ambiguous.

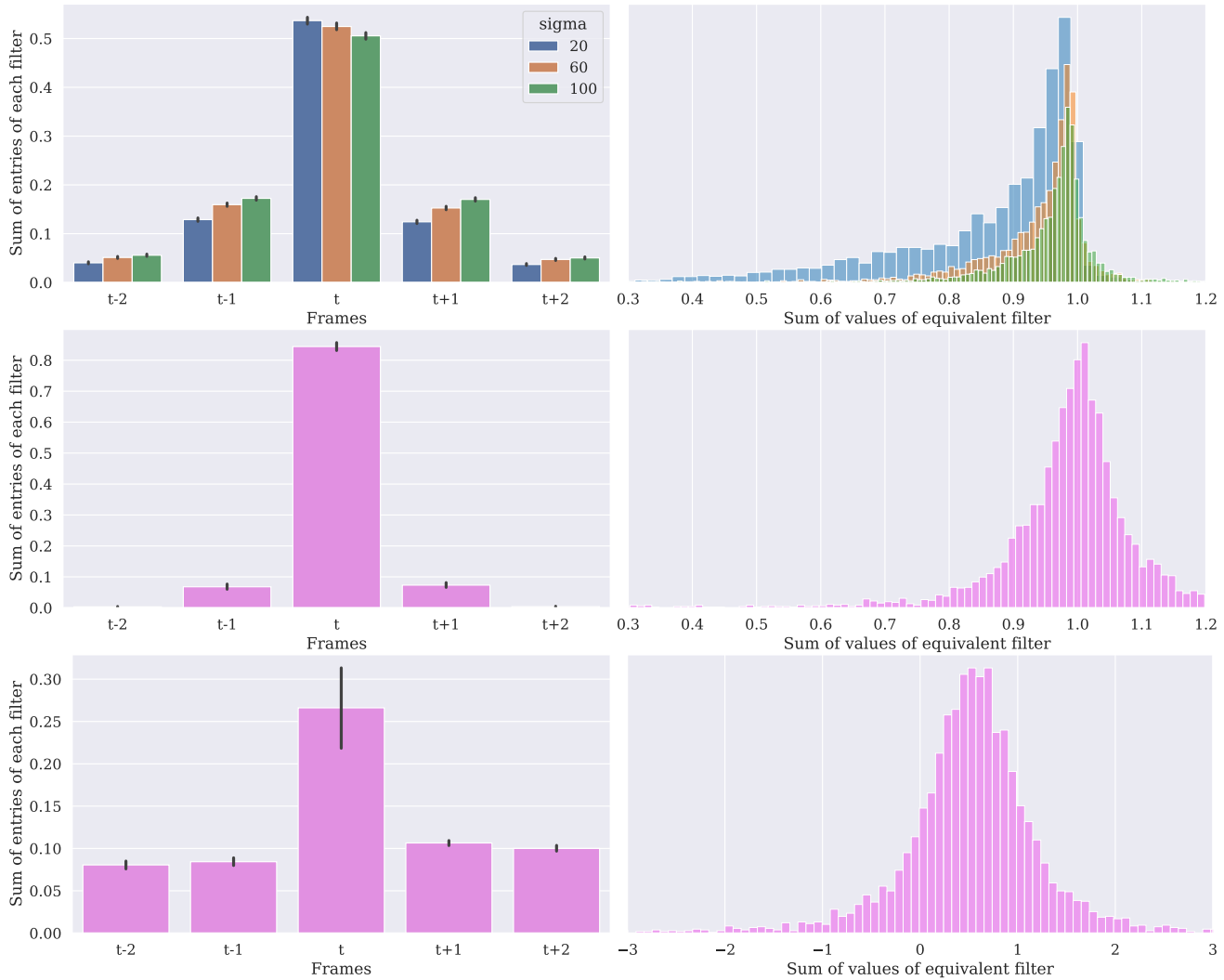


Figure 8. **Quantitative analysis of equivalent filters.** *Left column:* The graphs show the sum of the entries of the equivalent filters in each frame, averaged over 5000 pixels from 250 random patches of size 128×128 . For all datasets, the central frame dominates. For the DAVIS dataset (top), the contribution from the other frames increases with the noise level. For the fluorescence-microscopy data (mid) the contribution of the other frames is rather low, due to the high signal-to-noise ratio. For the electron-microscopy dataset the contribution of the other frames is larger (bottom). *Right column:* Histogram of the sum of all entries in the equivalent filters (over all 5 frames) for 5000 pixels from 250 random patches of size 128×128 from the DAVIS test set (top), the fluorescence-microscopy dataset (mid) and the electron-microscopy dataset (bottom). For the DAVIS and fluorescence-microscopy datasets, the filters sum to 1 in most cases. The peak of electron microscopy deviates significantly from 1. This could be due to the noise model, which has non-Gaussian characteristics (it is Poisson with low counts).



Figure 9. **Video denoising as spatiotemporal adaptive filtering; giant-slalom video from the DAVIS dataset.** Visualization of the linear weighting functions ($a(k, i)$, Section 7 of paper) of UDVD. The left two columns show the noisy frame y_t at four levels of noise, and the corresponding denoised frame, d_t . Weighting functions $a(k, i)$ corresponding to the pixel i (at the intersection of the dashed white lines), for five successive frames, are shown in the last five columns. The weighting functions adapt to underlying image content, and are shifted to track the motion of the skier. As the noise level σ increases, their spatial extent grows, averaging out more of the noise while respecting object boundaries. The weighting functions corresponding to the five frames approximately sum to one, and thus compute a local average (although some weights are negative, depicted in blue) as explained in Section F.1.

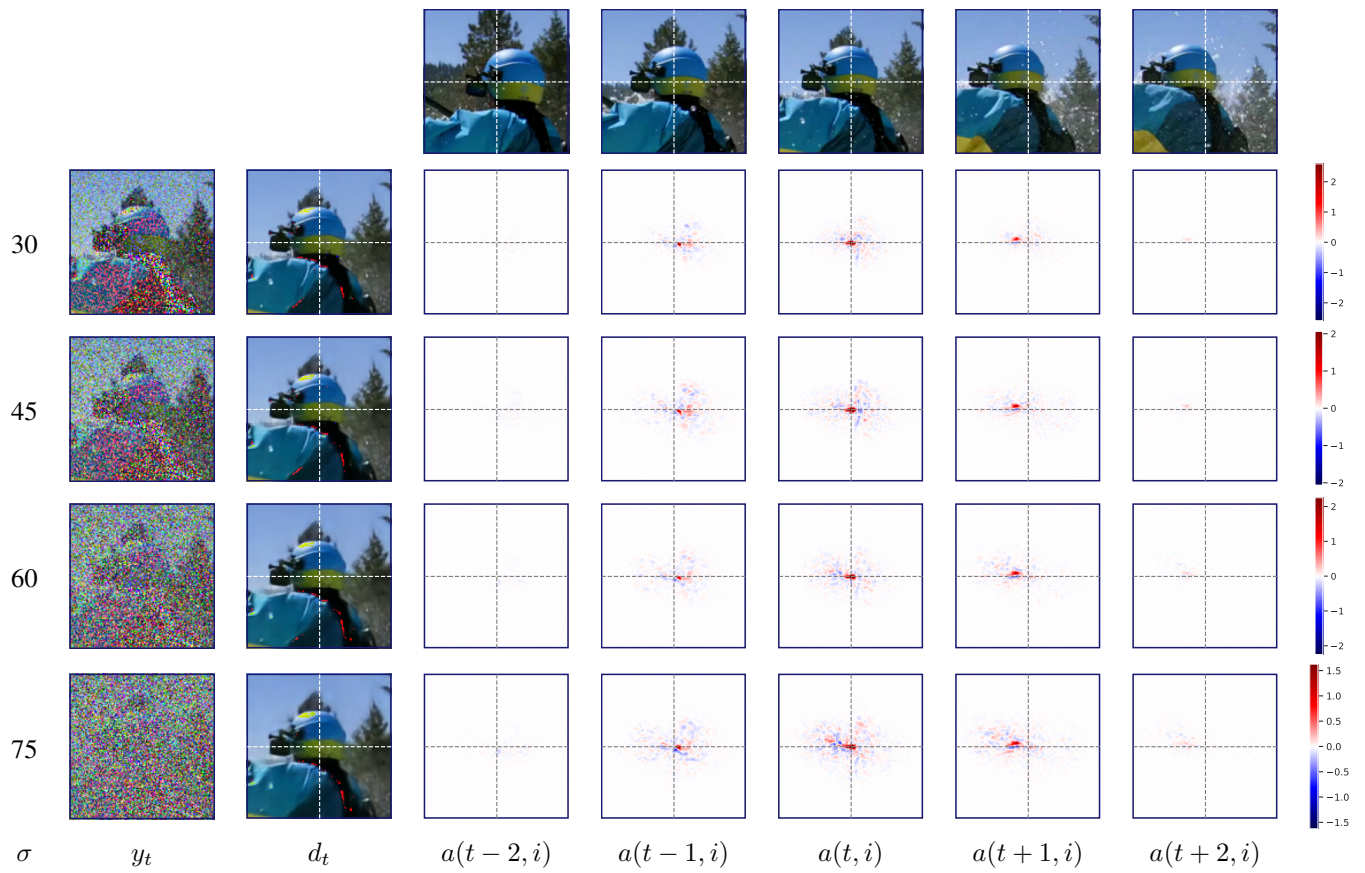


Figure 10. Video denoising as spatiotemporal adaptive filtering; rafting video from the GoPro dataset. Visualization of the equivalent filters, as described in Fig 9.

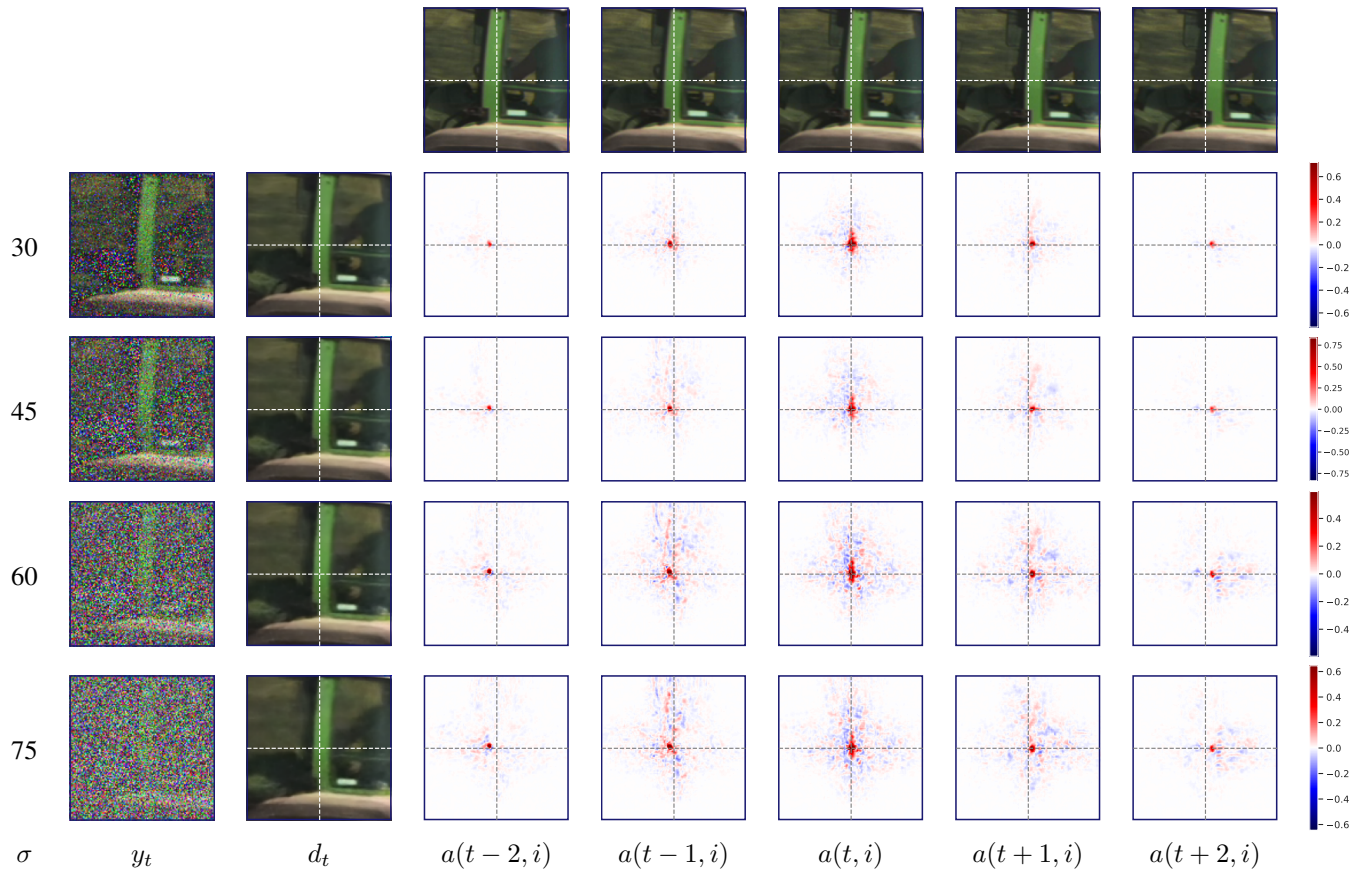


Figure 11. Video denoising as spatiotemporal adaptive filtering; **tractor** video from Set8. Visualization of the equivalent filters, as described in Fig 9.

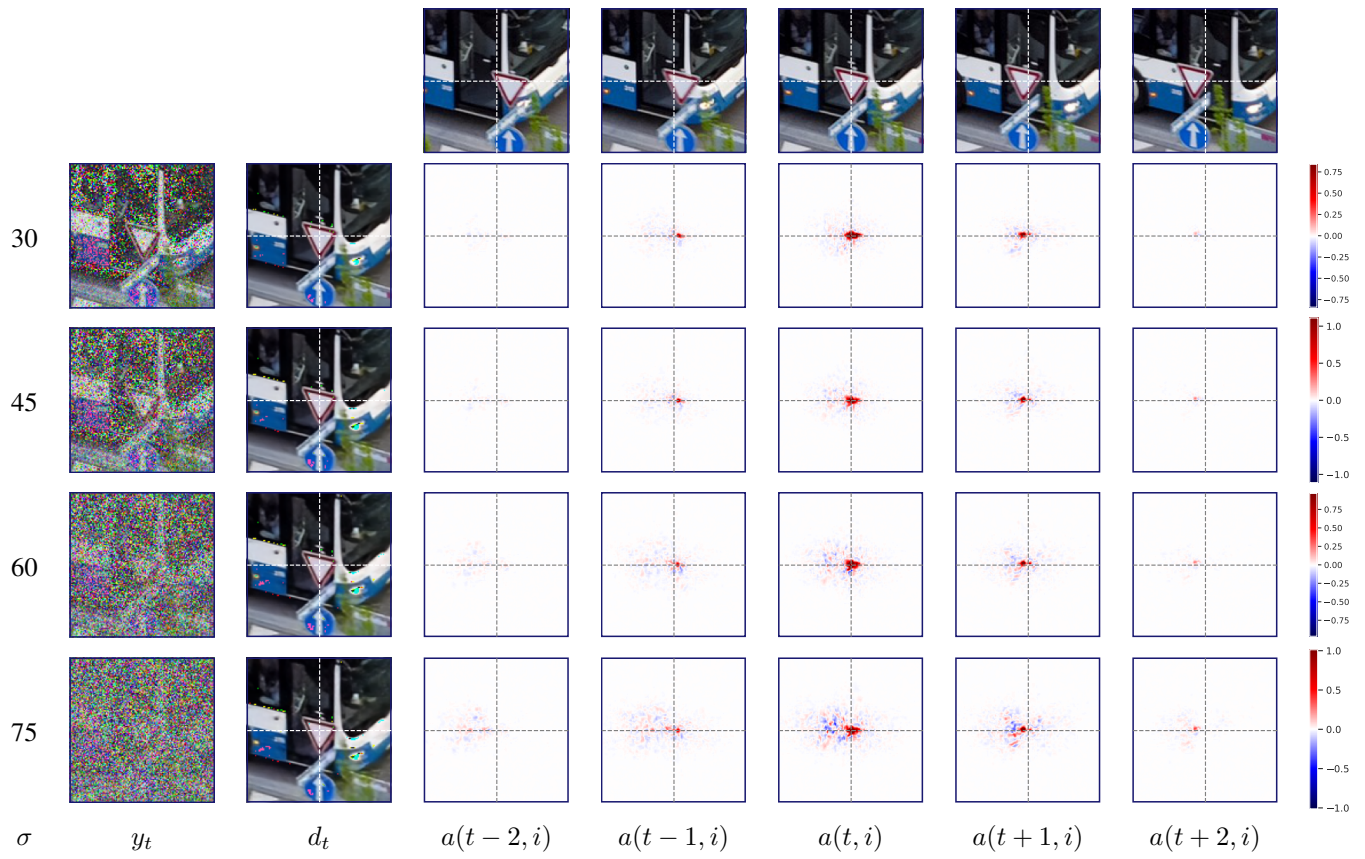


Figure 12. Video denoising as spatiotemporal adaptive filtering; bus video from the DAVIS dataset. Visualization of the equivalent filters, as described in Fig 9.

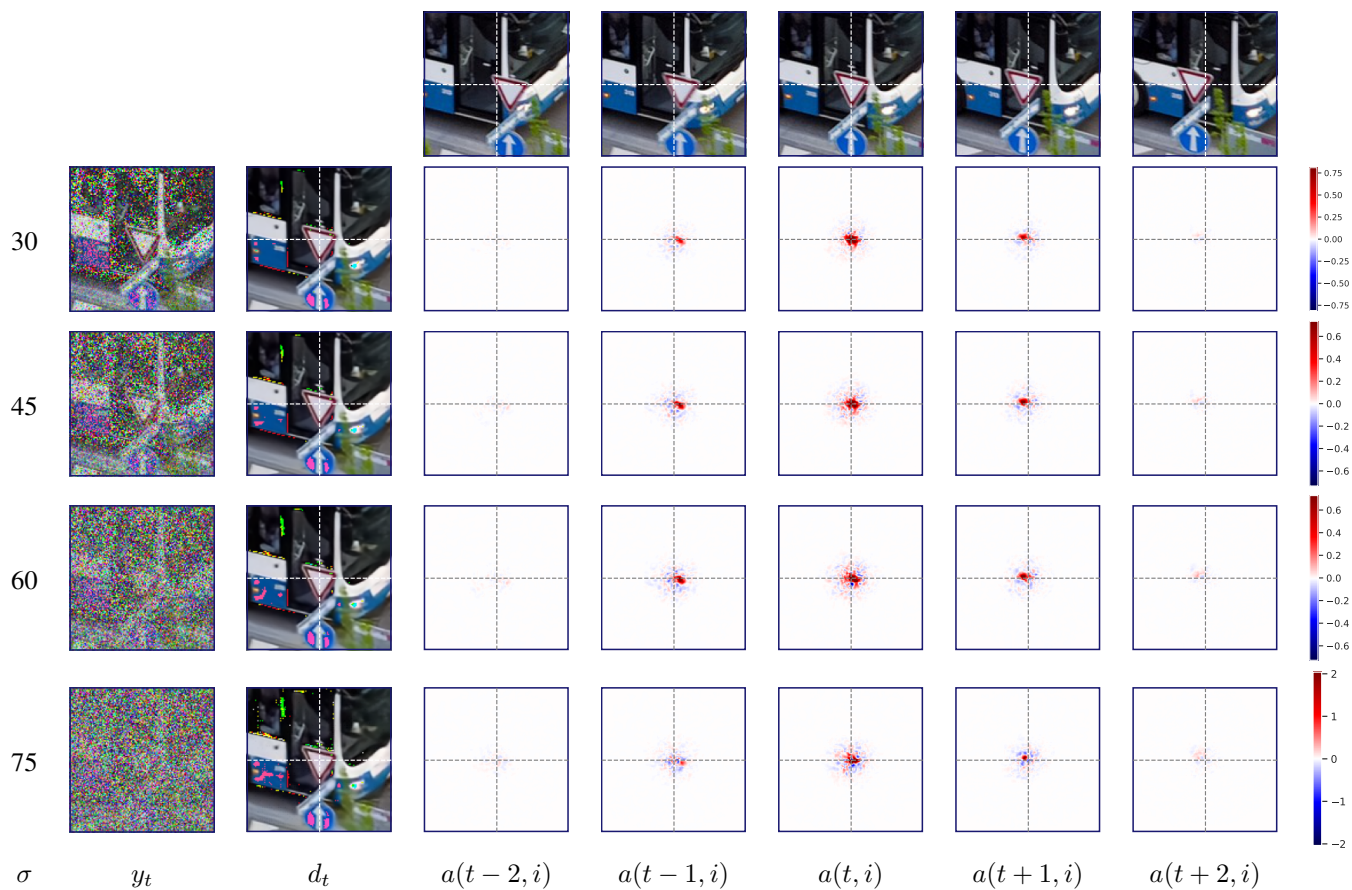


Figure 13. **Video denoising using FastDVDnet as spatiotemporal adaptive filtering; bus video from the DAVIS dataset.** Visualization of the linear weighting functions ($a(k, i)$, Section 7 of paper) of FastDVDnet which is trained with supervision. The left two columns show the noisy frame y_t at four levels of noise, and the corresponding denoised frame, d_t . Weighting functions $a(k, i)$ corresponding to the pixel i (at the intersection of the dashed white lines), for five successive frames, are shown in the last five columns. The weighting functions adapt to underlying image content, and are shifted to track the motion of the stop sign. As the noise level σ increases, their spatial extent grows, averaging out more of the noise while respecting object boundaries. The behavior is very similar to the corresponding filters of UDVD as shown in Fig 12.

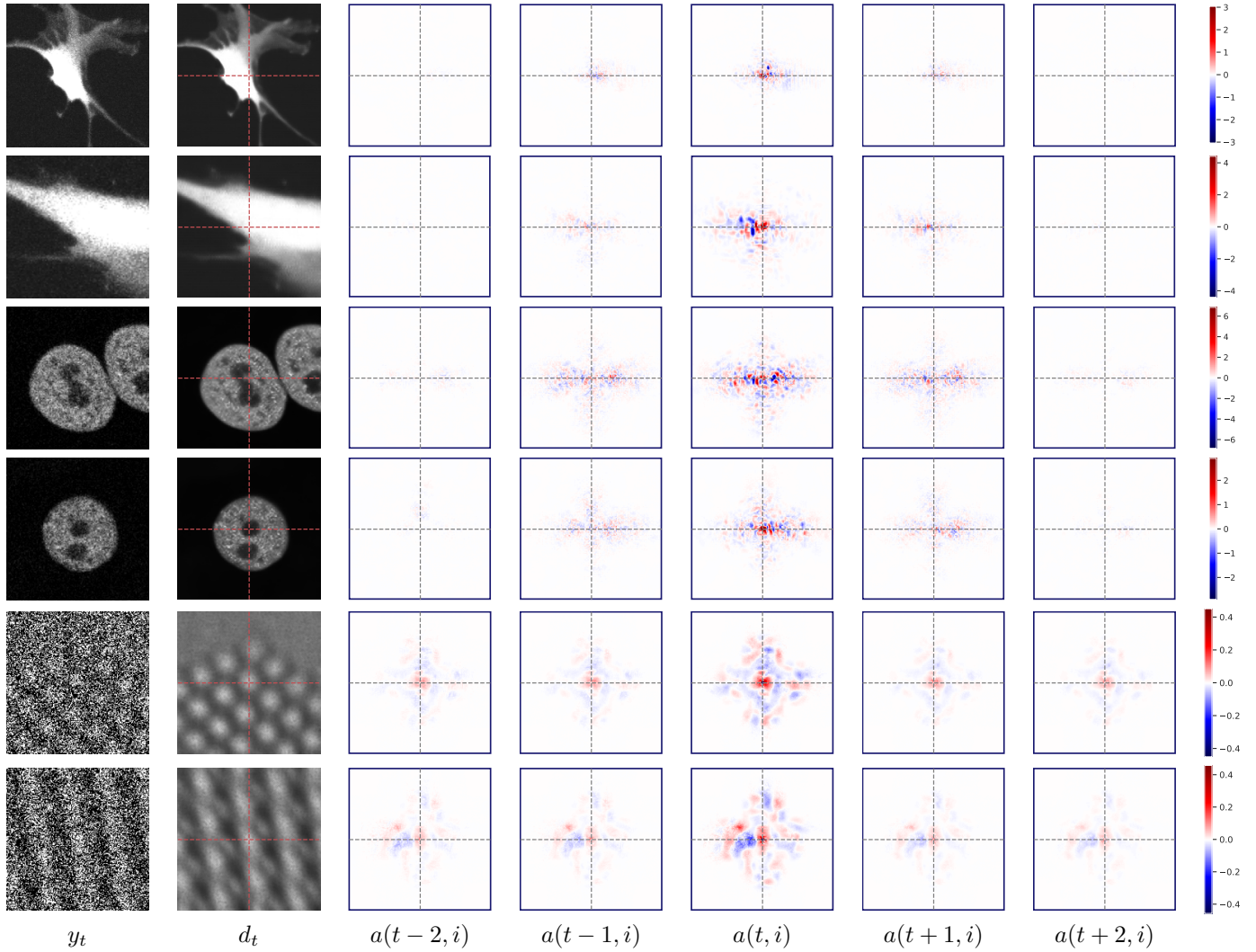


Figure 14. **Equivalent filters of UDVD when applied to microscopy data.** Visualization of the linear weighting functions ($a(k, i)$, Section 7 of paper) of UDVD trained to denoise fluorescence and electron microscopy data. The left two columns show the noisy frame y_t and the corresponding denoised frame, d_t . Weighting functions $a(k, i)$ corresponding to the pixel i (at the intersection of the dashed white lines), for five successive frames, are shown in the last five columns. In the fluorescence-microscopy data, the contributions from neighbouring frames are smaller. For electron-microscopy data they are larger (see also Fig 8).

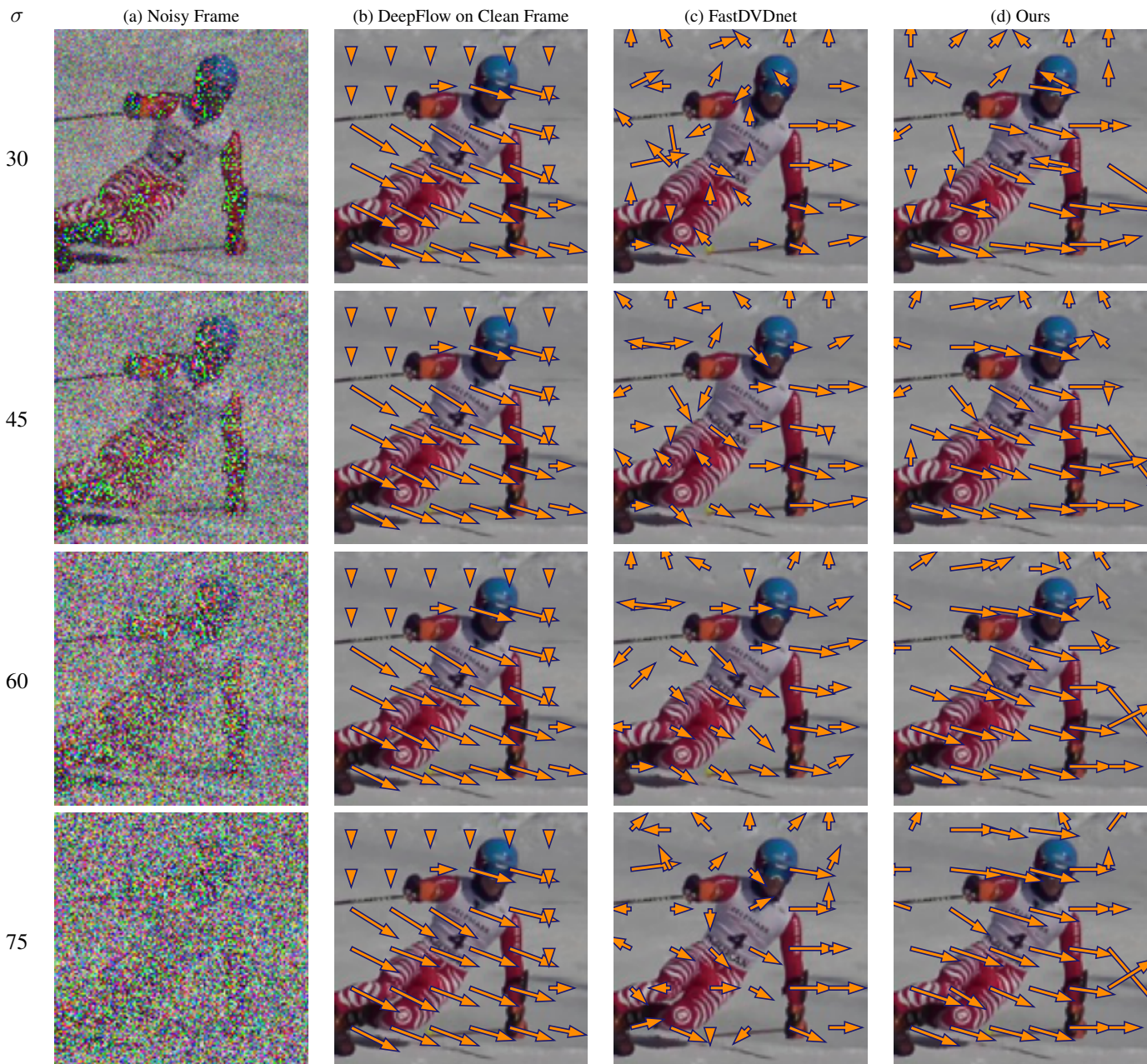


Figure 15. CNNs trained for denoising automatically learn to perform motion estimation. (a) Noisy frame from giant-slalom video in the DAVIS dataset. (b) Optical flow direction at multiple locations of the image obtained using a state-of-the-art algorithm applied to the clean video. Optical flow direction estimated from the shift of the adaptive filter obtained from the gradients of (c) FastDVDnet and (d) UDVD, both of which are trained with no optical flow information. FastDVDnet is trained with supervision. Optical flow estimates are well-matched to those in (b), but are not as accurate at oriented features, and in homogeneous regions where local motion is not well defined (e.g. in the background). Each row corresponds to a different noise levels. At higher noise levels, the networks perform averages over more frames, improving the motion estimation results.

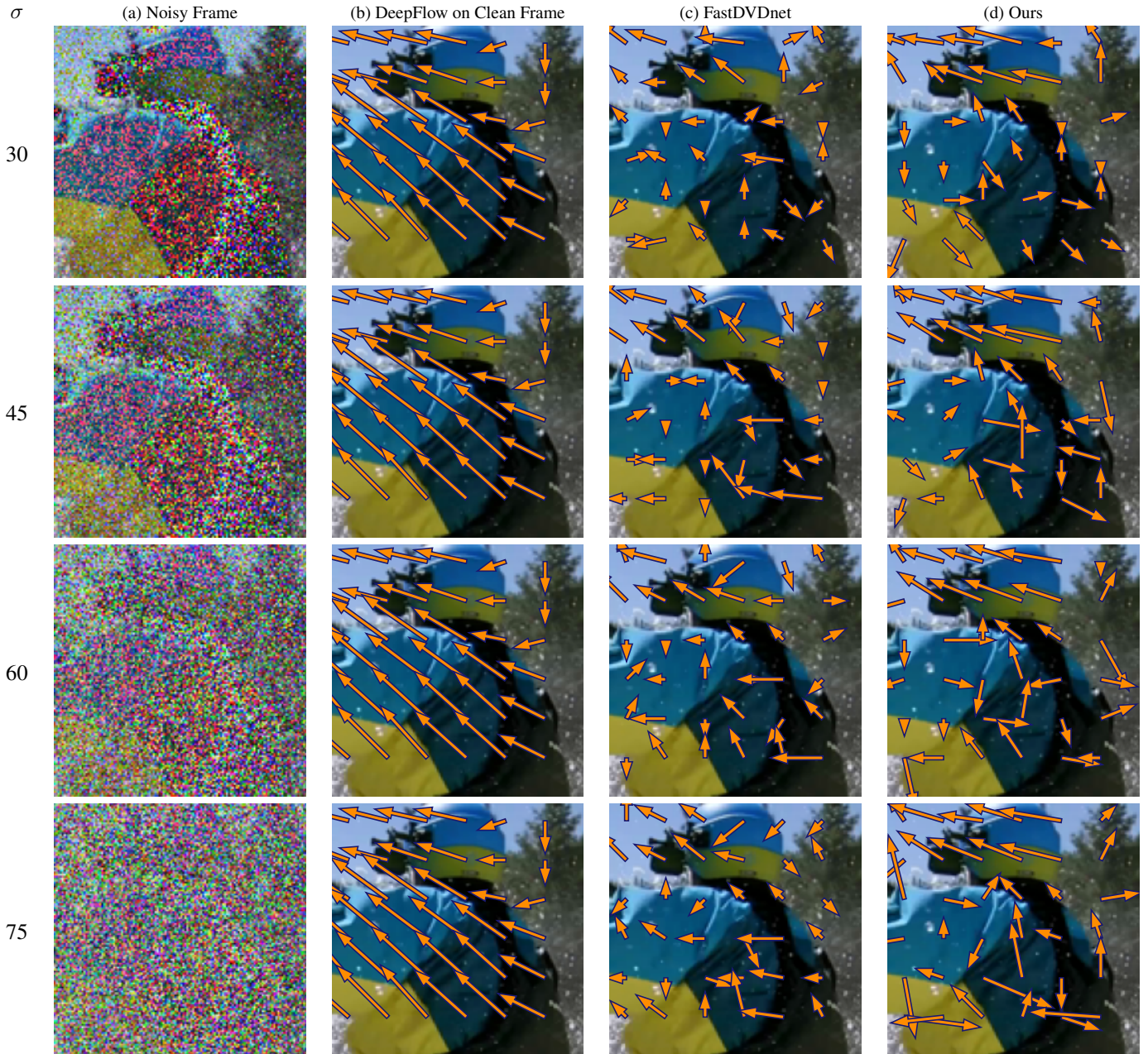


Figure 16. CNNs trained for denoising automatically learn to perform motion estimation; rafting video from Set8. Motion estimated from the gradients of UDVD and FastDVDnet. See description of Figure 15.

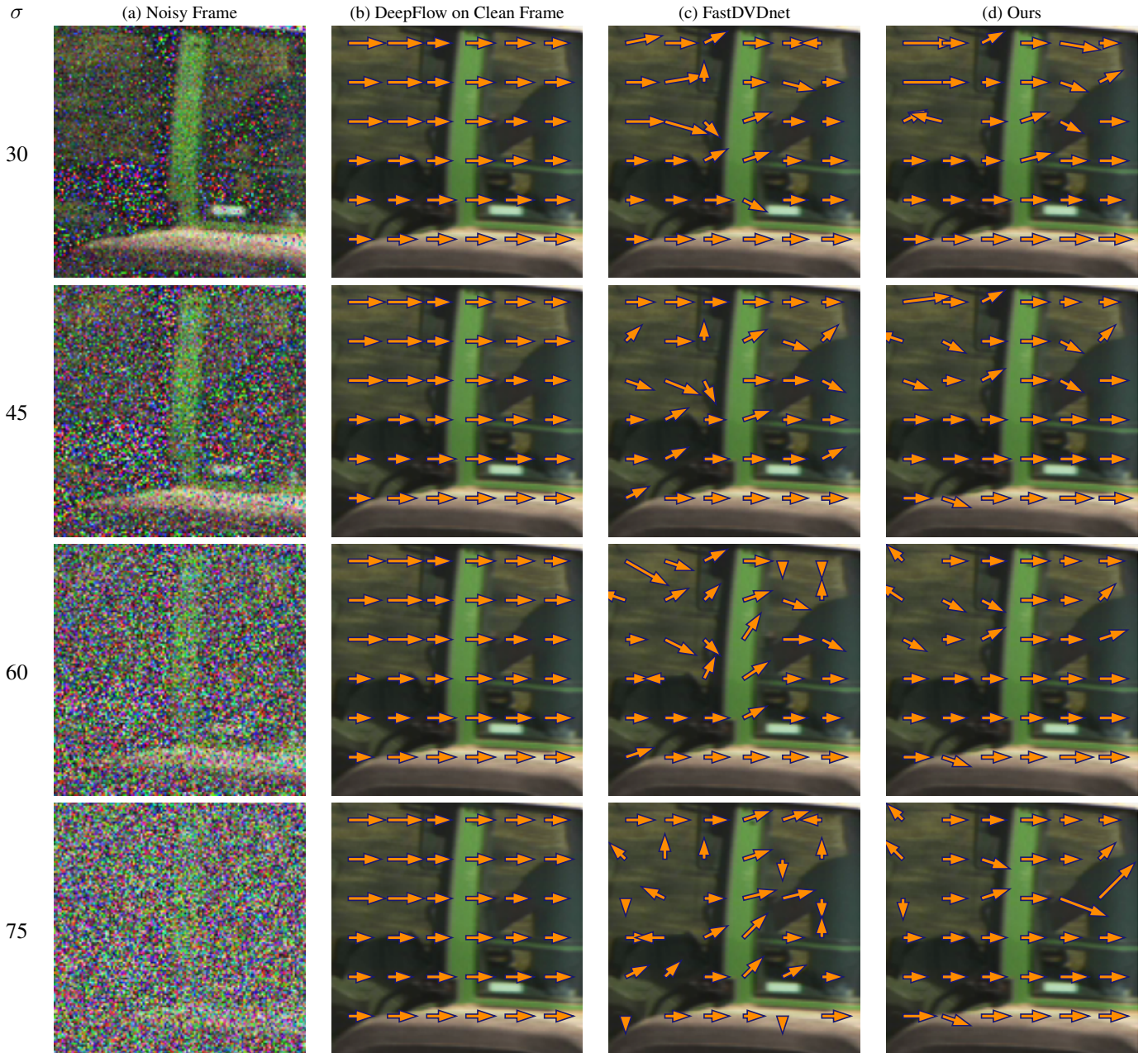


Figure 17. CNNs trained for denoising automatically learn to perform motion estimation; tractor video from Set8. Motion estimated from the gradients of UDVD and FastDVDnet. See description of Figure 15.

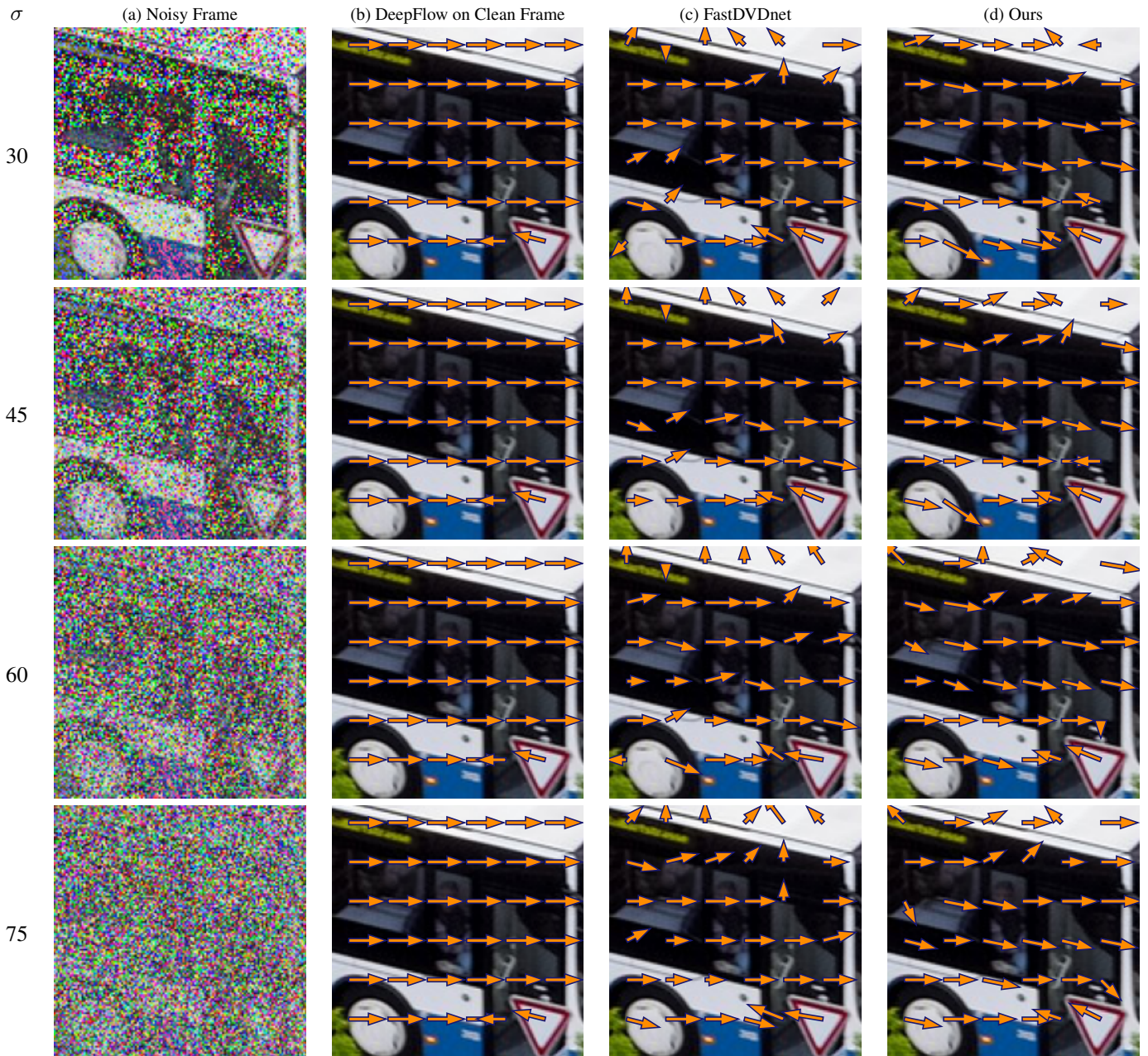


Figure 18. CNNs trained for denoising automatically learn to perform motion estimation; bus video from the DAVIS dataset. Motion estimated from the gradients of UDVD and FastDVDnet. See description of Figure 15.

Supplementary Material for Unsupervised Deep Video Denoising Paper ID 7679

A Implementation Details of Unsupervised Deep Video Denoising

A.1 Restricting field of view

In UDVD, we rotate the input frames by multiples of 90° and process them through four separate branches (with shared parameters) containing asymmetric convolutional filters that are *vertically causal*. As a result, the branches produce outputs that only depend on the pixels above (0° rotation), to the left (90°), below (180°) or to the right (270°) of the output pixel. We use a UNet [?] style architecture for each branch of UDVD. The field of view of the UNet is constrained by restricting the field of view of the convolutional, downsampling and upsampling layers that are used to build the UNet.

Convolutional Layers: We restrict the receptive field of each convolutional layer to extend only upwards following the strategy proposed in [?]. Let the filter size be $h \times w$. We zero-pad the top region of the input tensor with $k = \lfloor h/2 \rfloor$ zero rows before convolution and remove the bottom k rows after convolution. This is equivalent to convolving with a filter, where all weights below the center row are zero, so that the field of view only extends upwards.

Downsampling and Upsampling Layers: Following [?] we restrict the receptive field of the downsampling layer by creating an offset of one pixel (zero-pad with a row of zeros on the top and remove a row of pixels from below) before performing max-pooling using a 2×2 kernel. This operation restricts the field of view of the downsampling and upsampling operation pair.

Note that we do not use BatchNorm [?] layers in UDVD as computing the spatial mean and variance would modify the field of view to include the center pixel.

A.2 Adding the Noisy Pixel Back

The denoised generated by the proposed architecture at each pixel is computed without using the noisy observation at that location. This avoids overfitting – i.e. learning the trivial identity map that minimizes the mean-squared error cost function – but ignores important information provided by the noisy pixel. In the case of Gaussian additive noise, we can use this information via a precision-weighted average between the network output and the noisy pixel value. Following [?], the weights in the average are derived by assuming a Gaussian distribution for the error in the blind-spot estimates of the (color) pixel values. The CNN architecture is trained to estimate the mean and covariance of this distribution at each pixel by maximizing the log likelihood of the noisy data. We explain this in detail in the following paragraphs.

UDVD estimates the value of a pixel based on the noisy pixels in its neighbourhood. We model the distribution of the three color channels of a pixel $x \in \mathcal{R}^3$ given the noisy neighbourhood Ω_y as $p(x|\Omega_y) = \mathcal{N}(\mu_x, \Sigma_x)$, where $\mu_x \in \mathcal{R}^3$ and $\Sigma_x \in \mathcal{R}^3$ represent the mean vector and covariance matrix. Let $y = x + \eta$, $\eta \sim \mathcal{N}(0, \sigma^2 I_3)$ be the observed noisy pixel. We integrate the information in the noisy pixel with the UDVD output by computing the mean of the posterior $p(x|y, \Omega_y)$, given by

$$E[x|y] = (\Sigma_x^{-1} + \sigma^{-2}I)^{-1}(\Sigma_x^{-1}\mu_x + \sigma^{-2}y). \quad (1)$$

Note that the posterior mean has a very intuitive interpretation. When the signal variance is high compared to noise variance (i.e. the uncertainty in our estimation is high) the posterior mean favours noisy pixel value. We estimate μ_x and Σ_x as a function of the neighbourhood Ω_y using the network architecture discussed earlier. If x is a grayscale image, then the output of the network consists of two channels - one for μ_x and one for σ_x . When the input image has k channels, the output consists of k channels for μ_x and $k(k-1)/2$ for the upper-triangular entries of Σ_x .

One can estimate μ_x and Σ_x directly from the noisy data by maximizing the likelihood. Using our distributional assumptions, the noisy pixels y follows a Gaussian distribution, $y \sim \mathcal{N}(\mu_y, \Sigma_y)$, where $\mu_y = \mu_x$ and $\Sigma_y = \Sigma_x + \sigma^2 I$. Therefore, the loss function or the negative log likelihood is:

$$\mathcal{L}(\mu_x, \Sigma_x) = \frac{1}{2}[(y - \mu_x)^T(\Sigma_x + \sigma^2 I)^{-1}(y - \mu_x)] + \frac{1}{2} \log |\Sigma_x + \sigma^2 I|. \quad (2)$$

Name	N_{out}	Function
Input	k_1	
enc_conv_0	48	Convolution 3×3
enc_conv_1	48	Convolution 3×3
enc_conv_2	48	Convolution 3×3
pool_1	48	MaxPool 2×2
enc_conv_3	48	Convolution 3×3
enc_conv_4	48	Convolution 3×3
enc_conv_5	48	Convolution 3×3
pool_2	48	MaxPool 2×2
enc_conv_6	96	Convolution 3×3
enc_conv_7	96	Convolution 3×3
enc_conv_8	48	Convolution 3×3
upsample_1	48	NearestUpsample 2×2
concat_1	96	Concatenate output of pool_1
dec_conv_0	96	Convolution 3×3
dec_conv_1	96	Convolution 3×3
dec_conv_2	96	Convolution 3×3
dec_conv_3	96	Convolution 3×3
upsample_2	96	NearestUpsample 2×2
concat_2	$96+k_1$	Concatenate output of Input
dec_conv_4	96	Convolution 3×3
dec_conv_5	96	Convolution 3×3
dec_conv_6	96	Convolution 3×3
dec_conv_7	k_2	Convolution 3×3

Table 1: **Network architecture used for UDVD.** The convolution and pooling layers are the blind-spot variants described in Section A.1. k_1 and k_2 represent the number of input and output channels of the base network respectively.

If σ is unknown during training and has to be estimated, we use a separate neural network with the same architecture to do so. In such cases, we add a small regularization term equal to -0.1σ for numerical stability, following [?].

For the experiments with real data, the noise distribution is unknown, so we simply ignore the central pixel.

A.3 Architecture and Training

Architecture: The overall architecture is explained in Section 3 of the paper. The network architecture for the D1 and D2 blocks is described in Table 1. D1 has $k_1 = 9$ input channels and $k_2 = 32$ output channels. D2 has $k_1 = 96$ input channels and $k_2 = 96$ output channels. The architecture of D1 and D2 are analogous to the blocks in FastDVDnet [?] to facilitate fair comparison with the supervised models. As described in Fig. 2 of the paper, D2 is followed by a derotation and the output is passed to a series of three cascaded 1×1 convolutions and non-linearity for reconstruction with 4 and 96 intermediate output channels, as in [?]. The final convolutional layer is linear and has 9 output channels, 3 representing the RGB value of the denoised image and 6 representing its covariance matrix. We use the same architecture for fluorescence microscopy and electron microscopy with the number of input channels to UDVD modified to 5 and number of output channels modified to 1.

Training Details: Following the convention in image and video denoising, we train UDVD on 128×128 patches extracted from our dataset [? ? ? ? ?] (this is also consistent with the training methodology of the supervised baselines). For the natural video and fluorescence microscopy datasets, no data augmentation was applied. For electron microscopy dataset, we applied spatial flipping, time reversal and time subsampling (i.e. skipping frames).

Optimization Details: All networks were trained using Adam [?] optimizer with a starting learning of 10^{-4} . The learning rate was decreased by a factor of 2 at checkpoints [20, 25, 30] during a total training of 40 epochs. We did not experiment with other learning rate schedules such as cosine scheduling, which is a popular choice in unsupervised image denoising [?].

σ	DAVIS				Set8			
	Supervised CNN	Unsupervised CNN (UDVD)			Supervised CNN	Unsupervised CNN (UDVD)		
	5 frames	1 frame	3 frames	5 frames	5 frames	1 frame	3 frames	5 frames
20	35.86	33.98	34.75	34.99	33.37	32.20	32.97	33.25
30	34.06	32.79	33.42	33.86	31.60	30.68	31.46	31.86
40	32.80	31.47	32.15	32.61	30.37	29.33	30.18	30.62
50	31.83	30.46	31.15	31.63	29.42	28.28	29.18	29.63
60	30.97	29.63	30.33	30.84	28.75	27.44	28.36	28.82
70	30.16	28.94	29.64	30.16	28.00	26.75	27.66	28.14
80	29.20	28.35	29.05	29.58	27.20	26.16	27.06	27.55

Table 2: **Performance of UDVD.** Table shows the mean PSNR values of a state-of-the-art supervised video denoiser (FastDVDnet [?]) and UDVD with the denoised frame being predicted from $k \in \{1, 3, 5\}$ surrounding frames. The performance of UDVD monotonically increases with k and is comparable for supervised denoising across all noise levels. All the three UDVD networks reported here are trained for only $\sigma = 30$. FastDVDnet is trained for $\sigma \in [5, 55]$.

B Ablation Study on Number of Input Frames

We perform an ablation study on the number of frames k UDVD uses as input, $k \in \{1, 3, 5\}$. UDVD with $k = 1$ is equivalent to the blind-spot network proposed for image denoising in [?]. In this section we describe the architectural and training details for UDVD with $k \in \{1, 3, 5\}$ and present some additional results.

Architectural Details: UDVD with $k = 1$ contains only one UNet style network in each branch with architecture described in Table 1 and Section A.3. There are 3 input channels and 9 output channels (3 for the RGB channels in each denoised pixel and 6 for the corresponding covariance matrix). UDVD with $k = 3$ has a similar architecture as for $k = 1$ but has 9 input channels instead (3 channels for each frame). The architecture for $k = 5$ is described in Section A.3.

Training Details: UDVD with $k \in \{1, 3, 5\}$ was trained on the DAVIS dataset with $\sigma = 30$. The training details were as described in Section A.3.

Results: As shown in Table 1 of the paper and Table 2 performance improves substantially and monotonically with k (the number of surrounding frames used to denoise each frame) across a wide range of noise levels. This difference in performance can also be observed visually. Fig 1 shows an example where the texture details of the brick wall and the fence are not well recovered when using only a single noisy frame. The texture is estimated better when using 5 noisy frames to predict the denoised output.

C Denoising Results on Natural Video Datasets

In this section we provide additional comparisons between UDVD and supervised CNN-based methods.

1. Table 2 shows the performance of UDVD trained at $\sigma = 30$, and FastDVDnet trained for $\sigma \in [5, 55]$ when evaluated on the DAVIS test set and Set8 corrupted with $\sigma \in \{20, 40, \dots, 80\}$. UDVD achieves comparable performance to FastDVDnet on DAVIS test set and slightly outperforms it on Set8 at all noise levels.
2. Examples of noisy videos, and denoised counterparts obtained using UDVD are included in the attached zip file (hypermooth.mp4, rafting.mp4, motorbike.mp4 and snowboard.mp4).

D Denoising Results on Microscopy Video Datasets

The noisy fluorescence microscopy and electron microscopy data, and the denoised videos obtained with UDVD can be found in the supplementary zip file (fluoro_1.mp4, fluoro_2.mp4 and electron.mp4).

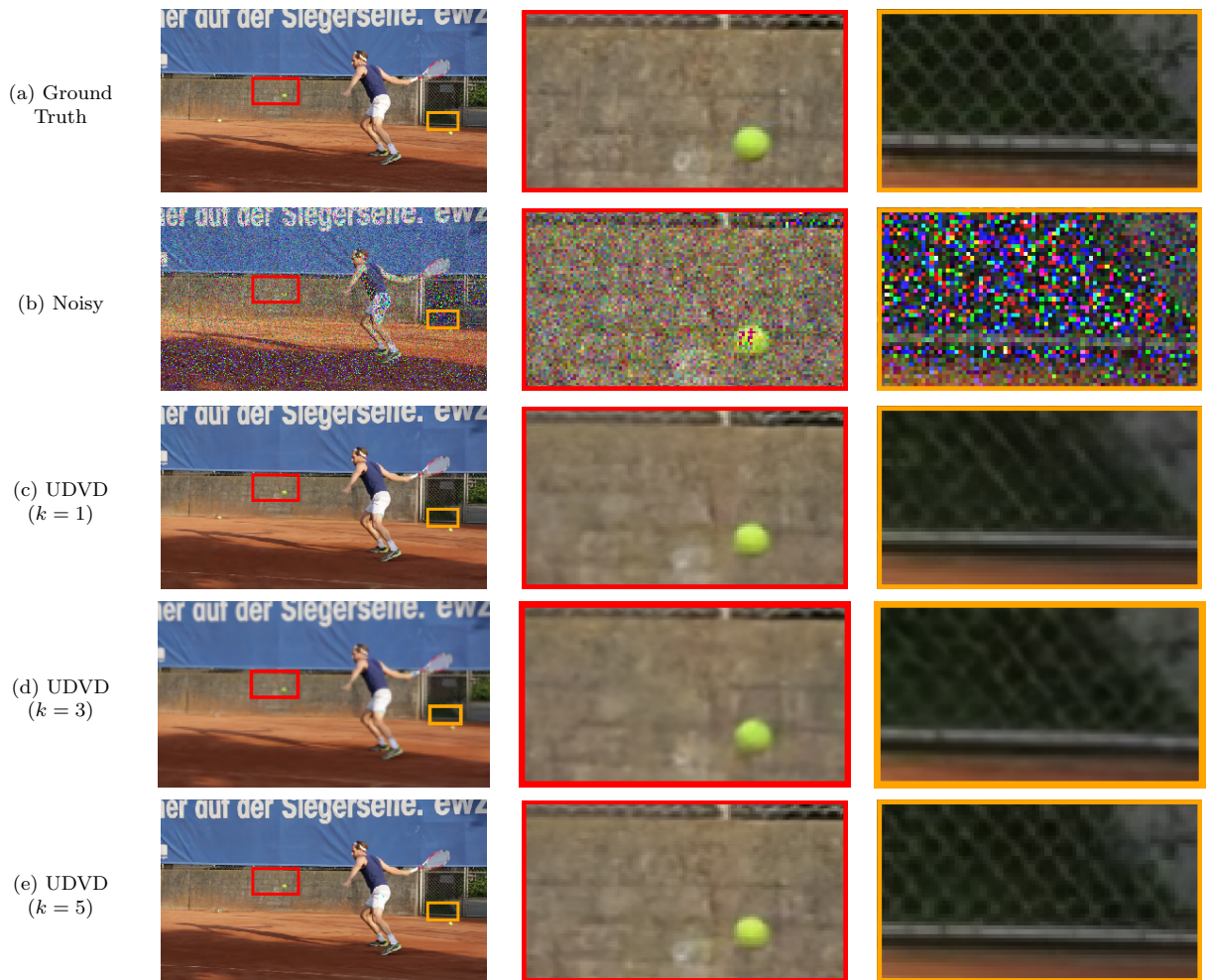


Figure 1: **Comparison of blind image and video denoising.** Example from the DAVIS dataset. (a) Ground truth frame. (b) Noisy frame. (c) Reconstruction using a single frame. The texture details of the brick wall and the fence are not recovered well. Reconstruction using (d) 3 and (e) 5 surrounding frames produces an improved texture estimate.

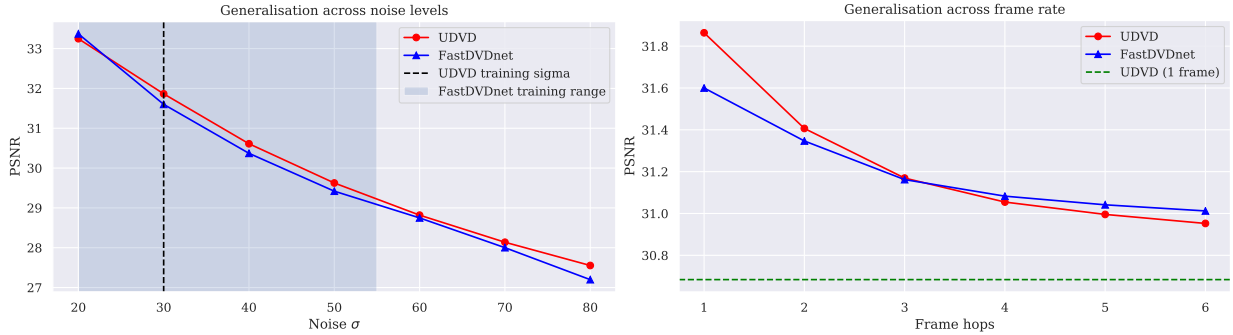


Figure 2: **Generalization across noise levels and frame rates.** (left) UDVD trained at only $\sigma = 30$ generalizes well to noise levels not seen during training. The plotted points represent mean PSNR values evaluated on Set8. (right) UDVD generalizes well to faster videos (created by skipping frames) and consistently outperforms a baseline image denoiser (UDVD with a single input frame, shown as a green dashed line).

E Generalization Across Noise and Frame Rate

Ideally, a denoiser should be able to denoise videos corrupted at a wide range of noise levels. This is usually achieved by training the CNN on examples corrupted with a range of noise strength [? ? ?]. The range of noise levels on which the network is trained is called the *training range* of the network.

Generalization outside the training range: The authors of [?] showed that CNNs trained for image denoising generalize well on test images corrupted with noise in the training range, but fails catastrophically when corrupted with noise strength outside the training range. The authors provided evidence that the overfitting is due to additive terms in the convolutional layers (and BatchNorm [?]) and showed that a CNN with no additive terms, called a *bias-free* CNN generalizes well outside the training range. UDVD uses a bias-free architecture and generalizes well to noise levels outside its training range (Fig 2).

Generalization across frame rates: To test generalization across frame rates, we simulated faster videos by skipping frames of videos in Set8. Fig 2 shows that UDVD generalizes robustly to faster videos and maintains a significant gain in performance over single-image denoising even when tested on videos where a large number of frames have been skipped (i.e. at a very low frame rate).

F Analysis of CNN-based Video Denoising

F.1 Natural Videos

In Section 7 and Fig 4 of the paper we examined the equivalent filters and illustrated that UDVD learns to denoise by performing an average over a spatiotemporal neighbourhood of each pixel. Here we examine equivalent filters for more videos and a supervised CNN (FastDVDnet) and show that similar observations hold.

Adaptive filtering: Fig 4, 5, 6 and 7 shows filters computed at a pixel for 4 different videos at 4 different noise levels. The filters adapt to the underlying signal content. They span larger areas as the noise level increases. These observations also holds for FastDVDnet, which is trained with supervision (Fig 8)

Contribution of neighbouring frames for denoising: UDVD tends to ignore temporally distant frames at lower noise levels as shown in Fig 4, 5, 6 and 7. This phenomenon is quantified in Fig 3 by plotting the contribution of each frame to the denoised pixel by averaging over **5000** pixels from **250** random patches of size 128×128 . At higher noise levels, UDVD seems to use distant frames more. This is consistent with the ablation study, which shows that for higher noise levels using more surrounding frames improves the denoising performance. Similar results hold for supervised CNN FastDVDnet, as shown in Fig 8.

Local Averaging: The weighting functions or equivalent filters perform an approximate averaging operation. They are mostly non-negative (although they do have some negative entries as depicted in blue in Fig 4, 5, 6 and 7) and they approximately sum up to one (see Fig 3).

F.2 Microscopy Data

Equivalent filters for the fluorescence-microscopy and the electron-microscopy data are shown in Fig 9. The fluorescence -microscopy data have a low noise level. As expected from the results on natural videos (see Section C), the weighting functions are mostly confined to the middle frame (as quantified in Fig 3). In the electron-microscopy dataset the weighting functions shows that the network relies on adjacent frames to estimate the denoised (as quantified in Fig 3).

F.3 Motion Estimation

Figures 4, 5, 6 and 7 show that the equivalent filters in adjoining frames are automatically shifted spatially to account for the movement of objects in the videos. We extracted motion information using the shift as explained in Section 7. Figures 10, 11, 12 and 13 show additional examples for UDVD and FastDVDnet. The estimated optical flow is mostly consistent with the estimated obtained by DeepFlow [?] applied on the clean videos. The motion estimates obtained from the equivalent filters tends to be less accurate for pixels near strongly correlated features or highly homogeneous regions where the local motion is ambiguous.

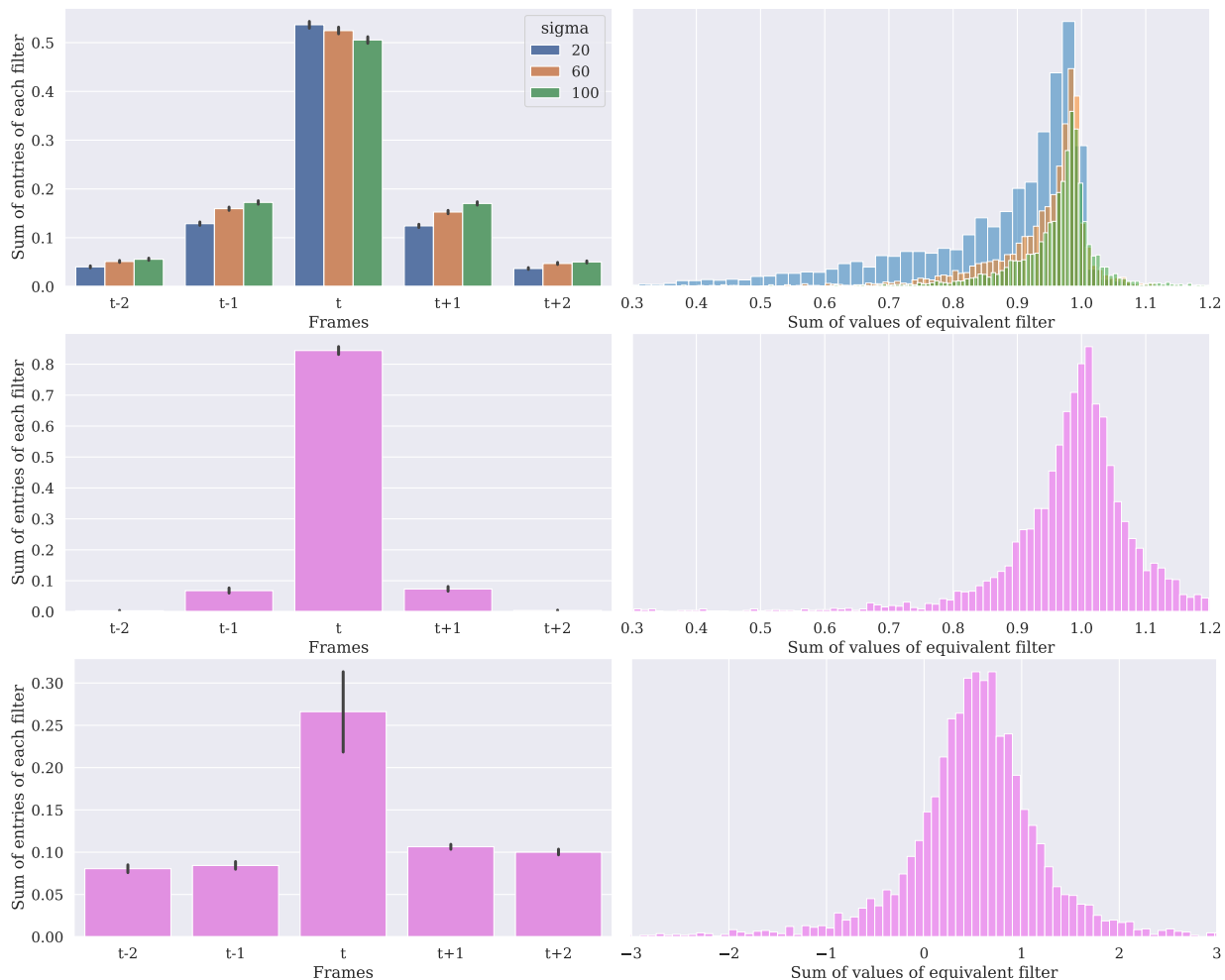


Figure 3: **Quantitative analysis of equivalent filters.** *Left column:* The graphs show the sum of the entries of the equivalent filters in each frame, averaged over 5000 pixels from 250 random patches of size 128×128 . For all datasets, the central frame dominates. For the DAVIS dataset (top), the contribution from the other frames increases with the noise level. For the fluorescence-microscopy data (mid) the contribution of the other frames is rather low, due to the high signal-to-noise ratio. For the electron-microscopy dataset the contribution of the other frames is larger (bottom). *Right column:* Histogram of the sum of all entries in the equivalent filters (over all 5 frames) for 5000 pixels from 250 random patches of size 128×128 from the DAVIS test set (top), the fluorescence-microscopy dataset (mid) and the electron-microscopy dataset (bottom). For the DAVIS and fluorescence-microscopy datasets, the filters sum to 1 in most cases. The peak of electron microscopy deviates significantly from 1. This could be due to the noise model, which has non-Gaussian characteristics (it is Poisson with low counts).

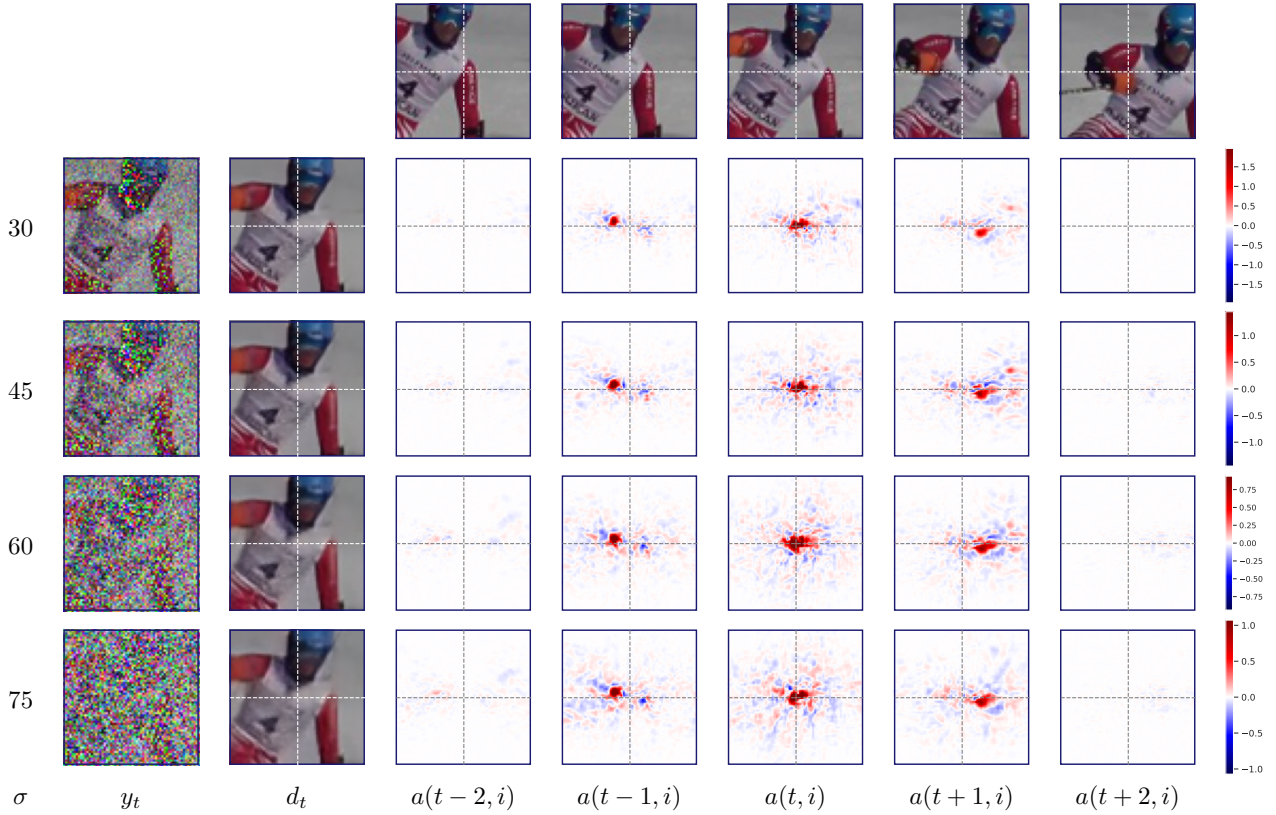


Figure 4: **Video denoising as spatiotemporal adaptive filtering; giant-slalom video from the DAVIS dataset.** Visualization of the linear weighting functions ($a(k, i)$, Section 7 of paper) of UDVD. The left two columns show the noisy frame y_t at four levels of noise, and the corresponding denoised frame, d_t . Weighting functions $a(k, i)$ corresponding to the pixel i (at the intersection of the dashed white lines), for five successive frames, are shown in the last five columns. The weighting functions adapt to underlying image content, and are shifted to track the motion of the skier. As the noise level σ increases, their spatial extent grows, averaging out more of the noise while respecting object boundaries. The weighting functions corresponding to the five frames approximately sum to one, and thus compute a local average (although some weights are negative, depicted in blue) as explained in Section F.1.

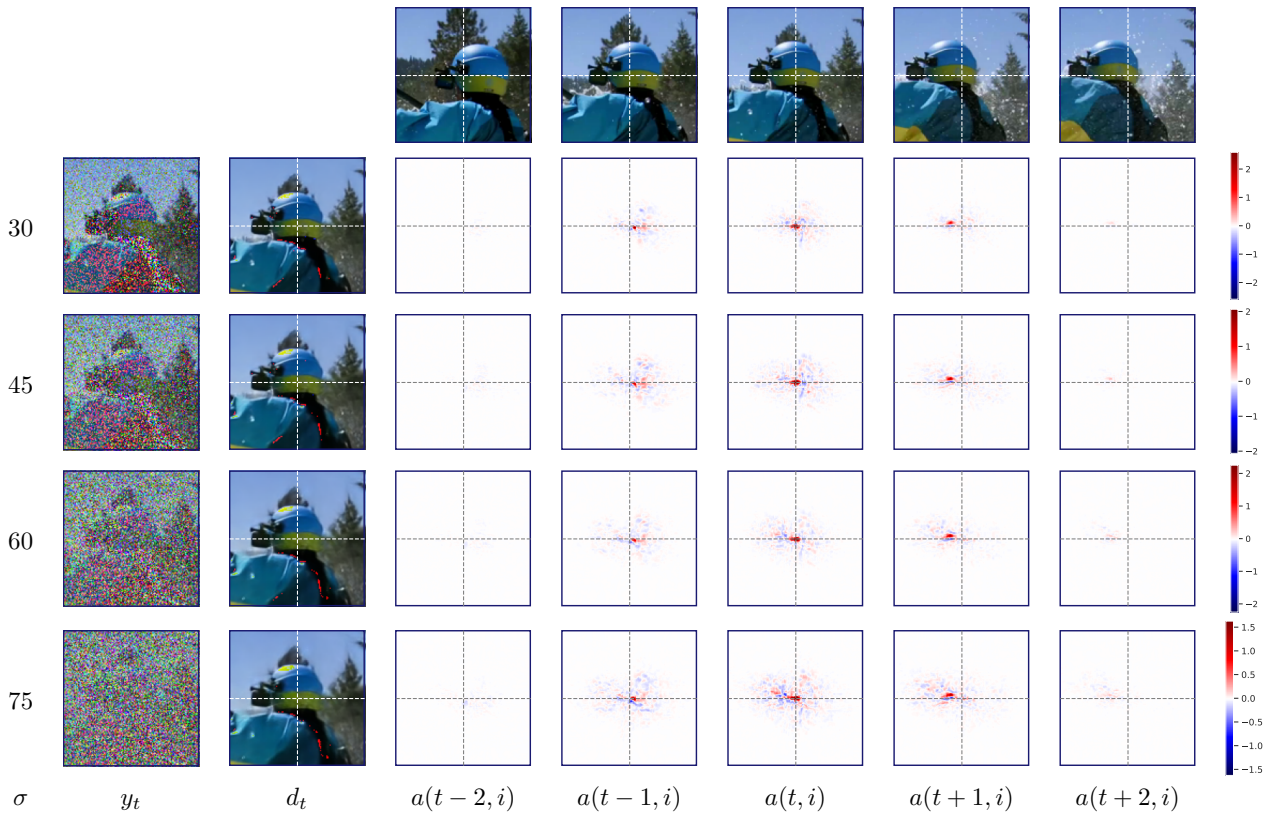


Figure 5: Video denoising as spatiotemporal adaptive filtering; rafting video from the GoPro dataset. Visualization of the equivalent filters, as described in Fig 4.

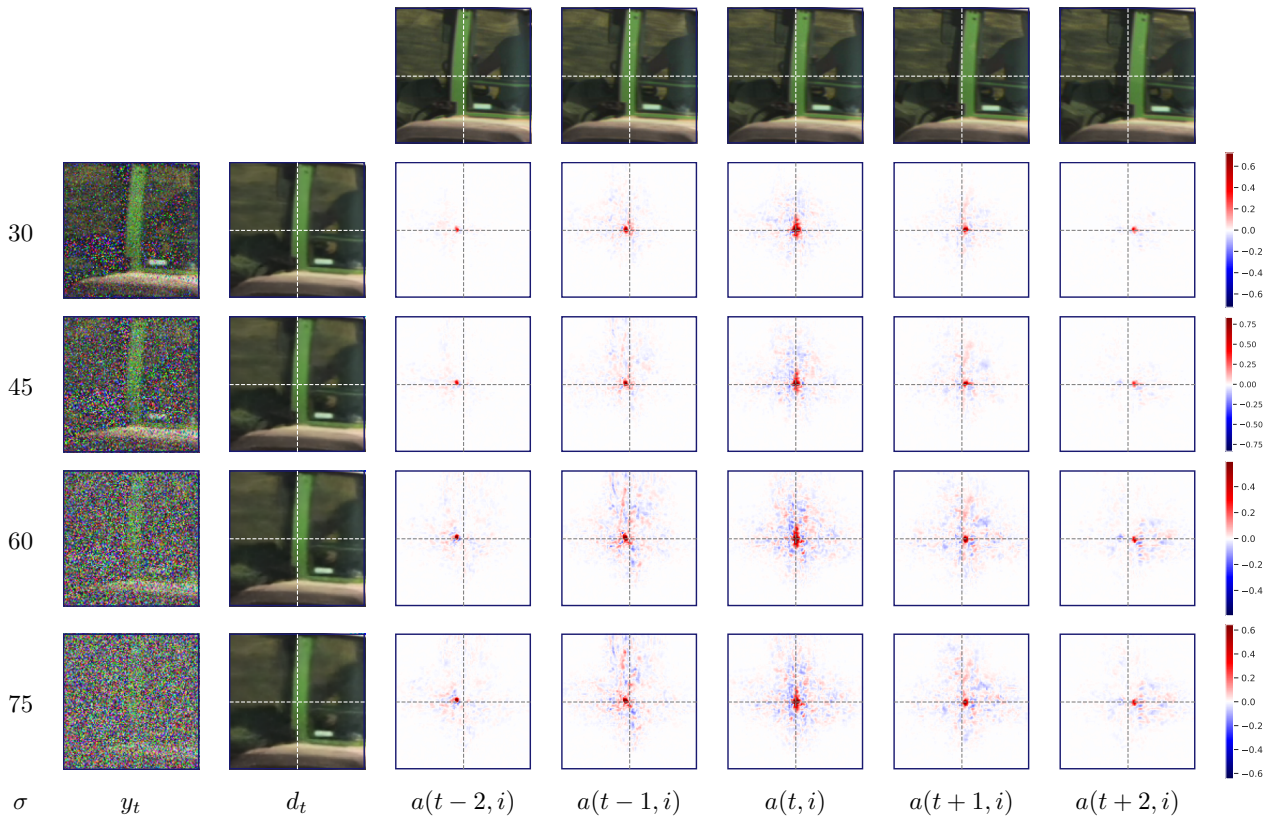


Figure 6: **Video denoising as spatiotemporal adaptive filtering; tractor video from Set8.** Visualization of the equivalent filters, as described in Fig 4.

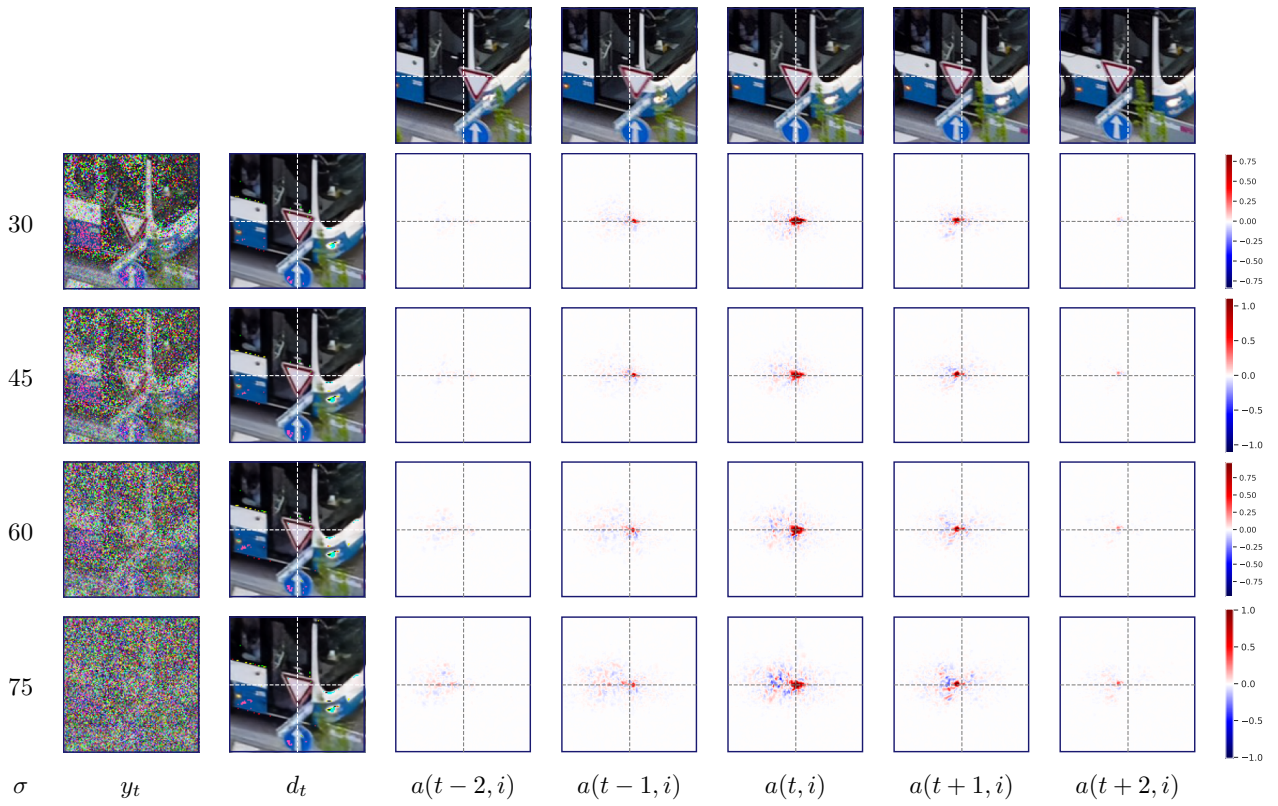


Figure 7: Video denoising as spatiotemporal adaptive filtering; bus video from the DAVIS dataset. Visualization of the equivalent filters, as described in Fig 4.

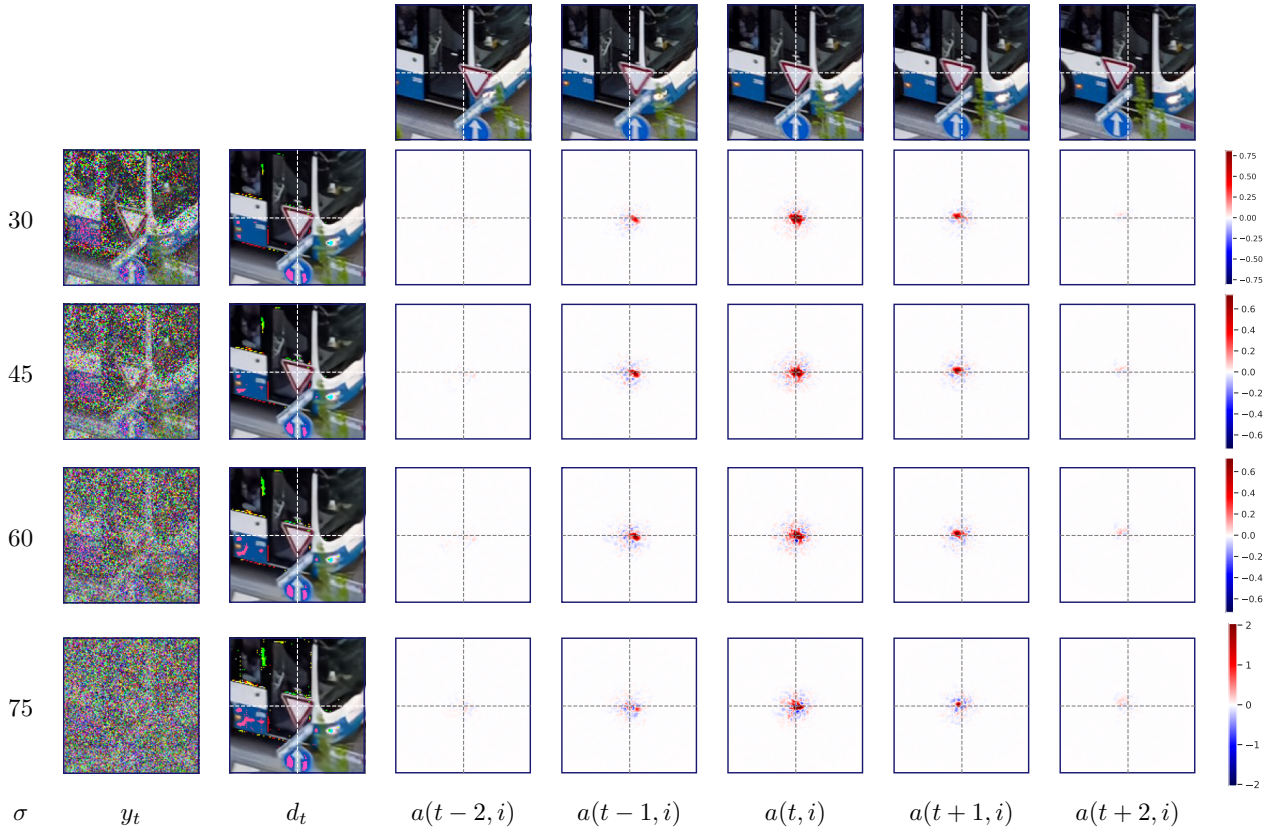


Figure 8: **Video denoising using FastDVDnet as spatiotemporal adaptive filtering; bus video from the DAVIS dataset.** Visualization of the linear weighting functions ($a(k, i)$, Section 7 of paper) of FastDVDnet which is trained with supervision. The left two columns show the noisy frame y_t at four levels of noise, and the corresponding denoised frame, d_t . Weighting functions $a(k, i)$ corresponding to the pixel i (at the intersection of the dashed white lines), for five successive frames, are shown in the last five columns. The weighting functions adapt to underlying image content, and are shifted to track the motion of the stop sign. As the noise level σ increases, their spatial extent grows, averaging out more of the noise while respecting object boundaries. The behavior is very similar to the corresponding filters of UDVD as shown in Fig 7.

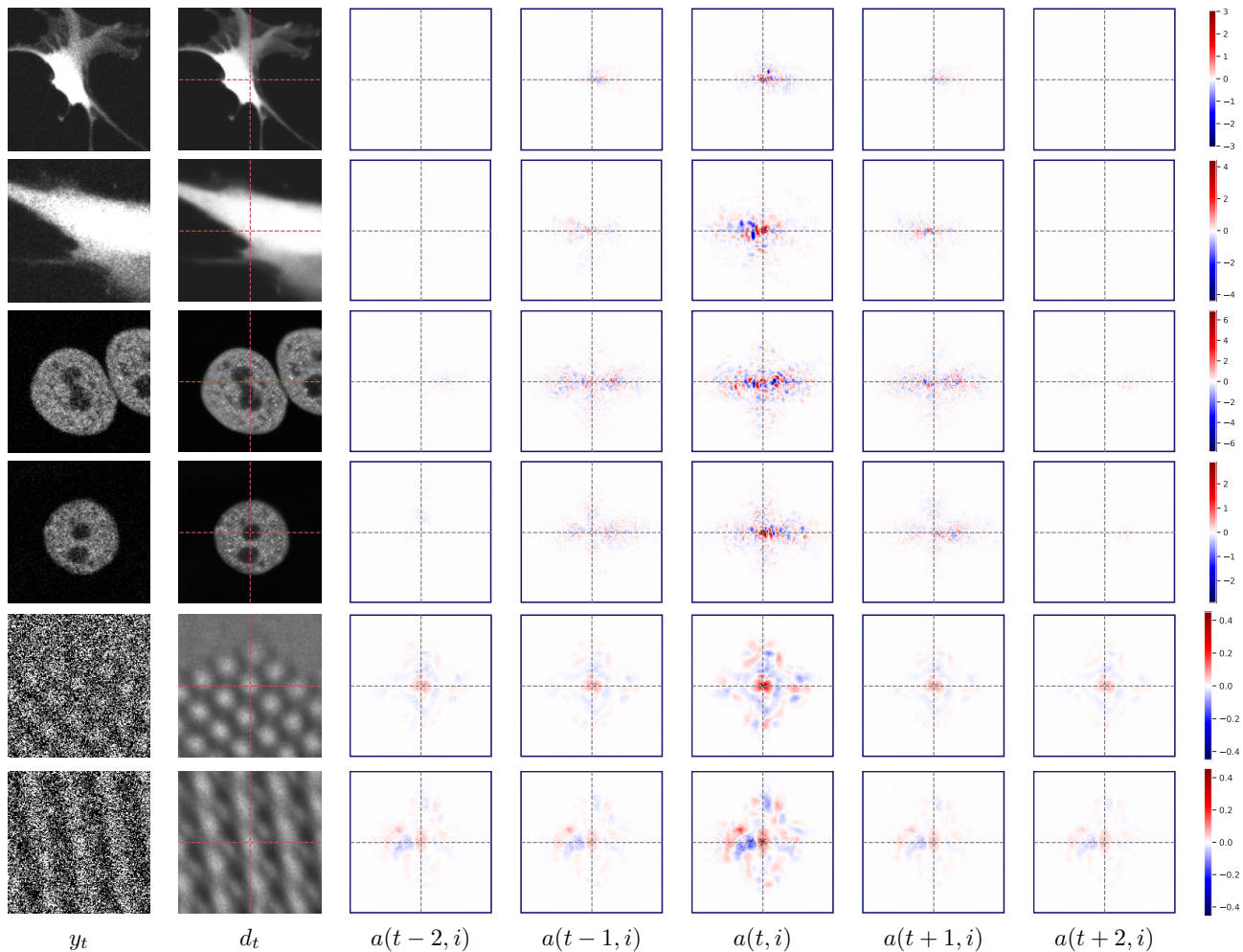


Figure 9: **Equivalent filters of UDVD when applied to microscopy data.** Visualization of the linear weighting functions ($a(k, i)$, Section 7 of paper) of UDVD trained to denoise fluorescence and electron microscopy data. The left two columns show the noisy frame y_t and the corresponding denoised frame, d_t . Weighting functions $a(k, i)$ corresponding to the pixel i (at the intersection of the dashed white lines), for five successive frames, are shown in the last five columns. In the fluorescence-microscopy data, the contributions from neighbouring frames are smaller. For electron-microscopy data they are larger (see also Fig 3).

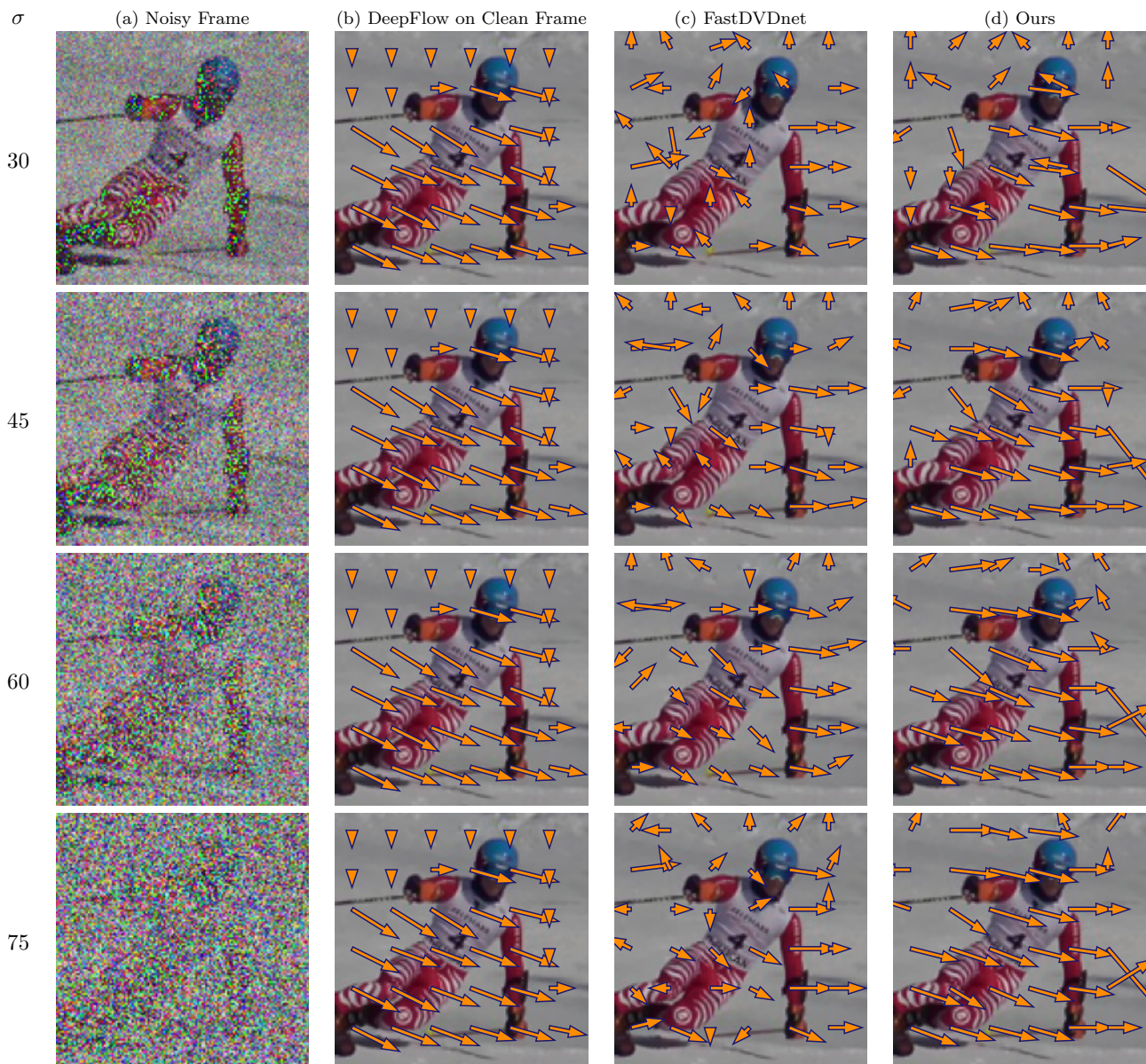


Figure 10: **CNNs trained for denoising automatically learn to perform motion estimation.** (a) Noisy frame from `giant-slalom` video in the DAVIS dataset. (b) Optical flow direction at multiple locations of the image obtained using a state-of-the-art algorithm applied to the *clean video*. Optical flow direction estimated from the shift of the adaptive filter obtained from the gradients of (c) FastDVDnet and (d) UDVD, both of which are trained with no optical flow information. FastDVDnet is trained with supervision. Optical flow estimates are well-matched to those in (b), but are not as accurate at oriented features, and in homogeneous regions where local motion is not well defined (e.g. in the background). Each row corresponds to a different noise levels. At higher noise levels, the networks perform averages over more frames, improving the motion estimation results.

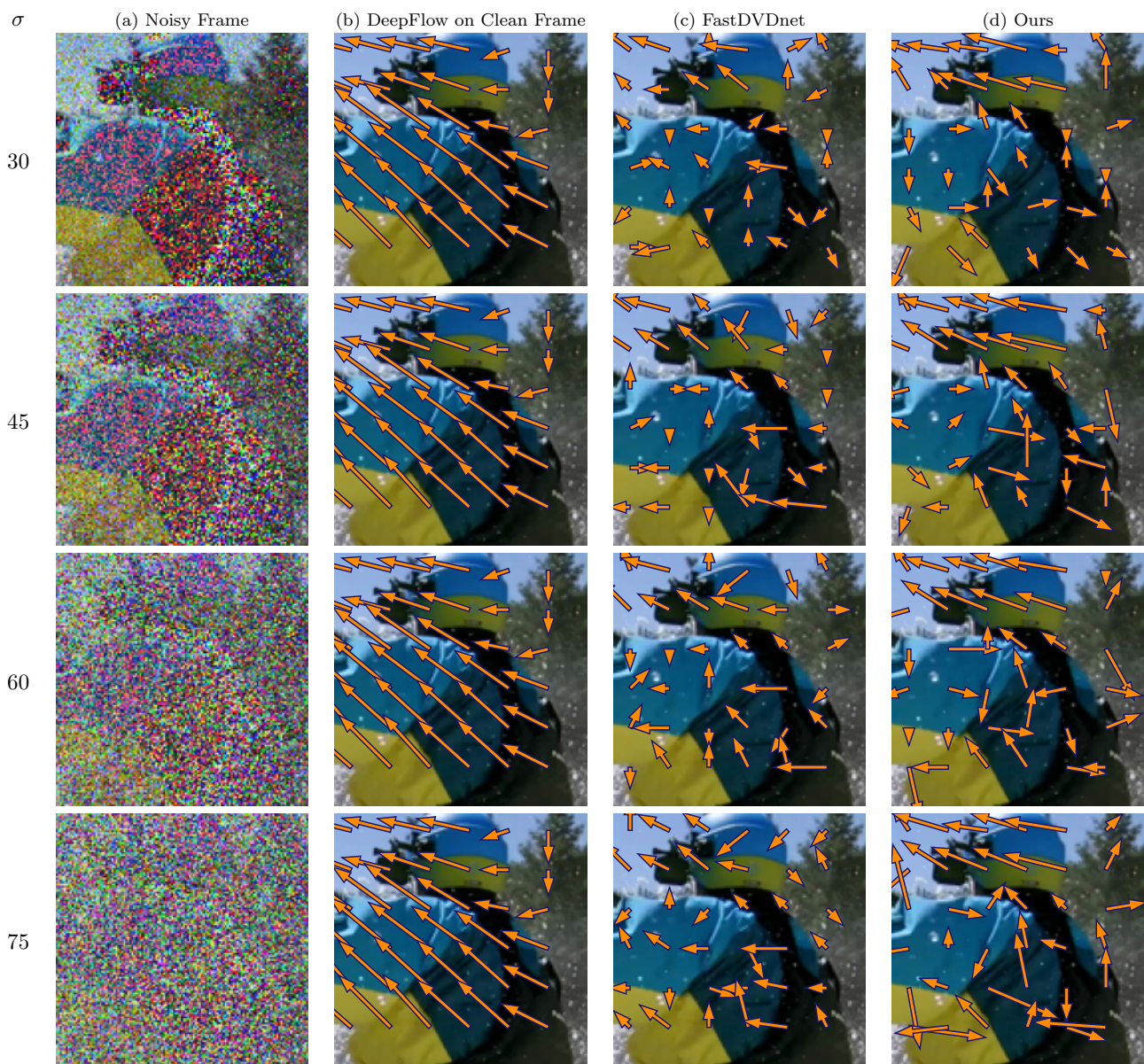


Figure 11: CNNs trained for denoising automatically learn to perform motion estimation; rafting video from Set8. Motion estimated from the gradients of UDVD and FastDVDnet. See description of Figure 10.

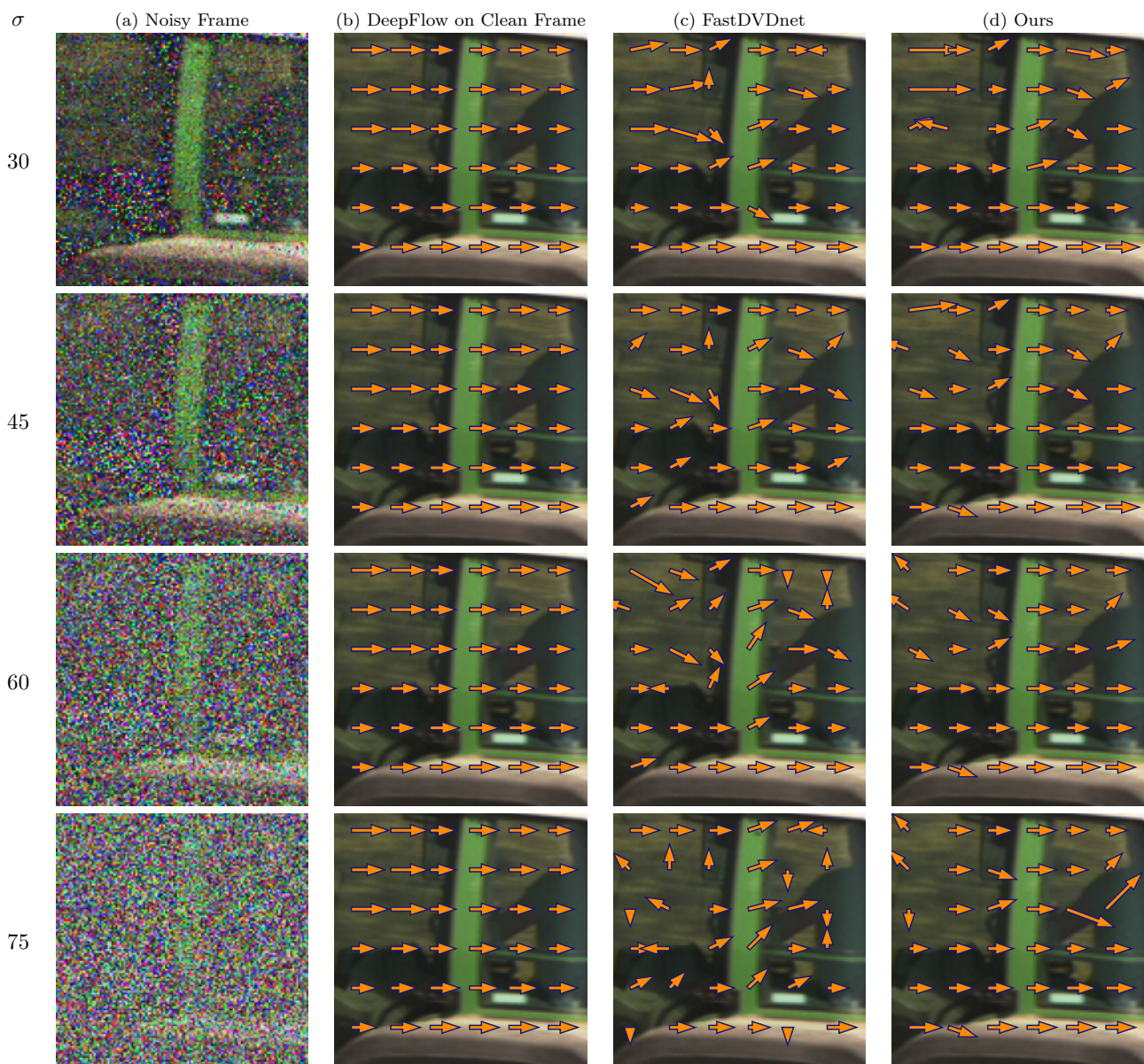


Figure 12: CNNs trained for denoising automatically learn to perform motion estimation; tractor video from Set8. Motion estimated from the gradients of UDVD and FastDVDnet. See description of Figure 10.

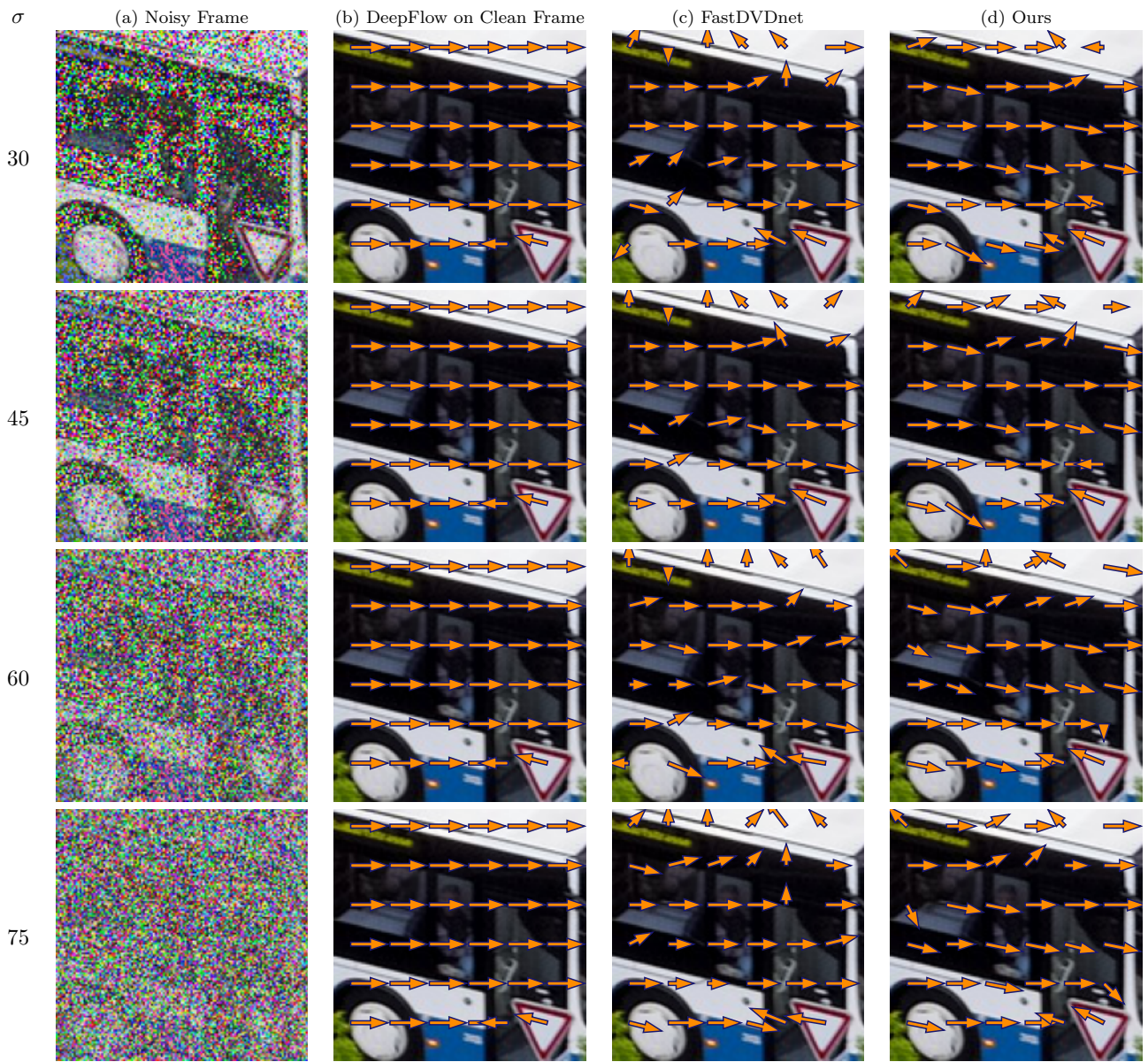


Figure 13: CNNs trained for denoising automatically learn to perform motion estimation; bus video from the DAVIS dataset. Motion estimated from the gradients of UDVD and FastDVDnet. See description of Figure 10.